Atmos. Chem. Phys., 18, 1923–1944, 2018
https://doi.org/10.5194/acp-18-1923-2018

Atmospheric Chemistry and Physics
Open Access
EGU

Atmospheric carbonyl sulfide (OCS) measured remotely by FTIR solar absorption spectrometry

Geoffrey C. Toon, Jean-Francois L. Blavier, and Keeyoon Sung

Jet Propulsion Laboratory, California Institute of Technology, Pasadena, California, USA

Correspondence: Geoffrey C. Toon (geoffrey.c.toon@jpl.nasa.gov)

Received: 30 April 2017 – Discussion started: 30 May 2017
Revised: 14 November 2017 – Accepted: 21 November 2017 – Published: 12 February 2018

Abstract. Atmospheric OCS abundances have been retrieved from infrared spectra measured by the Jet Propulsion Laboratory (JPL) MkIV Fourier transform infra-red (FTIR) spectrometer during 24 balloon flights and during nearly 1100 days of ground-based observations since 1985. Our spectral fitting approach uses broad windows to enhance the precision and robustness of the retrievals. Since OCS has a vertical profile similar in shape to that of N_2O, and since tropospheric N_2O is very stable, we reference the OCS observations to those of N_2O, measured simultaneously in the same air mass, to remove the effects of stratospheric transport, allowing a clearer assessment of secular changes in OCS. Balloon measurements reveal less than 5 % change in stratospheric OCS amounts over the past 25 years. Ground-based measurements reveal a springtime peak of tropospheric OCS, followed by a rapid early-summer decrease, similar to the behavior of CO_2. This results in a peak-to-peak seasonal cycle of 5–6 % of the total OCS column at northern mid-latitudes. In the long-term tropospheric OCS record, a 5 % decrease is seen from 1990 to 2002, followed by a 5 % increase from 2003 to 2012.

1 Introduction

With a column-averaged mole fraction of 450 ppt, OCS is the most abundant sulfur-containing gas in the atmosphere, except following major volcanic eruptions, when SO_2 can briefly dominate. OCS sources are at the surface: biogenic ocean activity produces OCS directly and also indirectly via oxidation of di-methyl-sulfide (DMS) and carbonyl sulfide (CS_2) (Kettle et al., 2002; Campbell et al., 2015). On land, the rayon industry emits CS_2, and there is evidence of biomass burning producing OCS which is lofted into the upper troposphere (Notholt et al., 2003).

The sinks of OCS are uptake by vegetation and soils, and at higher altitudes OCS is destroyed by OH and photolysis, leading to the formation of SO_2, which becomes a major source of non-volcanic SSA (stratospheric sulfate aerosol) (Crutzen, 1976; Wilson et al., 2008; Brühl et al., 2015). There is no consensus on the proportion of SSA that results from OCS versus direct volcanic injection of SO_2 (Leung et al., 2002). The SSA has an important impact on the radiation budget, transport, and chemistry (Crutzen, 1976). Its large surface area catalyzes heterogeneous reactions, some of which affect the stratospheric O_3 layer.

The ingestion of OCS by plants, similar to CO_2, is a diagnostic of the carbon cycle. The impact of biological activity on OCS abundance in the lower troposphere is (in fractional terms) much larger than CO_2. For example, the plant-induced seasonal cycle of CO_2 is about 2 % of the atmospheric column at northern mid-latitudes, whereas for OCS it is closer to 10 %. For tropospheric OCS it is 10–20 % (Campbell et al., 2008, 2015; Dlugokencky et al., 2001; Montzka et al., 2007). OCS is shorter-lived than CO_2 and with smaller sources, with the result that its atmospheric column is a million times smaller. The precision and accuracy of OCS measurements are therefore much poorer than those of CO_2.

OCS was first measured from space by the Atmospheric Trace Molecule Occultation Spectrometer (ATMOS) in 1985 (Zander et al., 1988). Since then, the ACE instrument has reported OCS measurements (Rinsland et al., 2007, 2008; Barkley et al., 2008). More recently, Glatthor et al. (2015, 2017) reported OCS profiles retrieved from spectra measured by the MIPAS instrument on board the ENVISAT satellite. Kuai et al. (2014, 2015) reported OCS column measurements

from the TES instruments on board the Aura satellite. Vincent and Dudhia (2017) reported OCS measurements from the IASI instrument.

Remote measurements of OCS from space promise new insights into the carbon cycle, provided that other factors that govern column OCS (e.g., stratospheric transport) can be correctly accounted for. CO_2 measurements alone can only determine net biosphere flux, but cannot differentiate between photosynthesis and respiration since these occur in the same locations. OCS is also taken up by plants during photosynthesis, but is not respired, and so may be able to help distinguish between these processes (Wang et al., 2016; Campbell et al., 2015). Plants have an equal affinity with CO_2 and OCS, in terms of their stomatal conductance and mesophyll diffusion, but the OCS has a 10 times higher biochemical activity (Berry et al., 2013).

The fact that OCS is shorter lived than CO_2 means that its vmr profile decreases more rapidly with altitude in the stratosphere. Thus stratospheric transport has far more impact on the total column amounts of OCS than CO_2, complicating attempts to accurately determine tropospheric OCS amounts from space. For example, if the OCS mole fraction were constant in the troposphere and decreased linearly with pressure above the tropopause, then a change in the tropopause altitude from 300 to 200 mbar (9 to 12 km) would result in a 5 % increase in the total OCS column above sea level. (For CO_2 a similar change in tropopause altitude would result in a 0.15 % change in the total column.) Such 5 % OCS variations are likely larger than the tropospheric variations of interest, e.g., due to exchange with the surface, especially in the Southern Hemisphere, where there is little land at mid-latitudes. So accounting/correcting for these stratospheric transport effects is an essential prerequisite for gaining insights into tropospheric OCS variations from total column measurements.

In this paper we show that the OCS and N_2O vmr profiles are similar in shape in the stratosphere and are strongly correlated, both being affected similarly by transport. Since the tropospheric N_2O amount varies very little, the N_2O total column can be used to account for transport-driven changes in the stratospheric OCS amount, allowing the tropospheric OCS behavior to be more clearly seen.

2 Methods

2.1 MkIV instrument

The MkIV FTS is a double-passed Fourier transform infrared (FTIR) spectrometer designed and built at the Jet Propulsion Laboratory (JPL) in 1984 for atmospheric observations (Toon, 1991). It covers the entire 650–5650 cm^{-1} region simultaneously with two detectors: a HgCdTe photoconductor covering 650–1800 cm^{-1} and an InSb photodiode covering 1800–5650 cm^{-1}. The MkIV instrument has flown 24 balloon flights since 1989. It has also flown on over 40 flights of the NASA DC-8 aircraft as part of various campaigns from 1987 to 1992 studying high-latitude ozone loss. MkIV has also made 1090 days of ground-based observations since 1985 from a dozen different sites, from Antarctica to the Arctic, from sea level to 3.8 km altitude. MkIV observations have been extensively compared with satellite remote sounders (e.g., Velazco et al., 2011) and with in situ data (e.g., Toon et al., 1999).

2.2 Analysis methods

The spectral fitting was performed with the Version 4.8 GFIT (Gas Fitting) code, a nonlinear least-squares algorithm developed at the JPL. GFIT scales user-prescribed a priori atmospheric gas vmr profiles to fit calculated spectra to those measured. For balloon observations, the atmosphere was discretized into 100 layers of 1 km thickness. For ground-based observations, 70 layers of 1 km thickness were used. Absorption coefficients were computed line-by-line assuming a Voigt lineshape and using the ATM linelist (Toon, 2014a) for the telluric lines. This is a "greatest hits" compilation, founded on HITRAN, but is not always the latest version for every band of every gas. In situations where the latest HITRAN version (Rothman et al., 2013) gave poorer fits, the earlier HITRAN version was retained. For OCS the ATM linelist is based on HITRAN 2012, but with 709 additional lines, empirically determined from laboratory spectra, representing missing hot-bands of the main isotopolog. The solar linelist (Toon, 2014b) used in the analysis of the ground-based spectra was obtained from analysis of low-air-mass spectra observed during balloon flights of the MkIV and shuttle flights of the ATMOS instruments.

Sen et al. (1996) provide a more detailed description of the use of the GFIT code for retrieval of vmr profiles from MkIV balloon spectra. GFIT was previously used for the Version 3 analysis (Irion et al., 2002) of spectra measured by ATMOS. It is currently used for analysis of TCCON spectra (Wunch et al., 2011) and MkIV spectra (Toon et al., 2016).

2.3 Balloon observations

The MkIV instrument has made 24 balloon flights since 1989. Several of these provided multiple occultations (e.g., sunset and sunrise during the same flight), so that in total we have 30 profiles, which are summarized in Table 1. The flights are predominantly from around 35° N, except for the 1997–2002 period when several high-latitude flights were undertaken from Fairbanks, Alaska, and Esrange, Sweden.

We measured OCS using five different windows (see Table 2). Those at 2050 and 2069 cm^{-1} cover the P- and R-branches of the ν_3 OCS band, which is 80 times stronger than any other OCS band. These ν_3 windows provide nearly all the stratospheric OCS information, but at lower altitudes these windows become increasingly blacked out (due to CO_2,

Table 1. Summary of MkIV balloon occultations. Lat. and Long. represent the latitudes and longitudes of the 20 km tangent point. Z_{min} and Z_{max} represent the altitudes over which the tangent altitude varied. Flights flagged by [a] or [b] in the Event column acquired no useful data.

Date	Lat. deg.	Long. deg.	Z_{min} km	Z_{max} km	Event	Launch site Town	State
5 Oct 1989	34.6	−105.3	13	37	Sunset	Ft. Sumner	New Mexico
27 Sep 1990	34.2	−105.6	10	36	Sunset	Ft. Sumner	New Mexico
5 May 1991	37.5	−111.5	15	37	Sunset	Ft. Sumner	New Mexico
6 May 1991	36.5	−113.0	15	32	Sunrise		
14 Sep 1992	35.2	−110.9	23	39	Sunset	Ft. Sumner	New Mexico
15 Sep 1992	35.3	−104.0	22	41	Sunrise		
3 Apr 1993	34.8	−114.8	17	37	Sunset	Daggett	California
25 Sep 1993	34.0	−107.5	6	38	Sunset	Ft. Sumner	New Mexico
26 Sep 1993	33.1	−95.3	13	38	Sunrise		
22 May 1994	36.1	−108.6	14	36	Sunset	Ft. Sumner	New Mexico
23 May 1994	36.3	−100.9	11	37	Sunrise		
24 Jul 1996	56.7	−100.9	11	24	Ascent[b]	Lynn Lake	Manitoba
28 Sep 1996	32.7	−113.1	4	38	Sunset	Ft. Sumner	New Mexico
8 May 1997	68.7	−146.0	8	38	Sunrise	Fairbanks	Alaska
8 Jul 1997	66.4	−148.3	7	32	Ascent	Fairbanks	Alaska
8 Jul 1997	64.7	−150.2	9	32	Descent		
3 Dec 1999	64.2	19.3	6	34	Sunset	Esrange	Sweden
15 Mar 2000	67.8	34.2	11	29	Sunrise	Esrange	Sweden
16 Dec 2002	64.4	31.2	12	31	Sunrise	Esrange	Sweden
1 Apr 2003	68.3	35.2	11	32	Sunrise	Esrange	Sweden
19 Sep 2003	34.3	−113.3	7	36	Sunset	Ft. Sumner	New Mexico
23 Sep 2004	33.8	−109.2	11	38	Sunset	Ft. Sumner	New Mexico
20 Sep 2005	35.2	−114.1	11	39	Sunset	Ft. Sumner	New Mexico
21 Sep 2005	34.0	−110.3	13	29	Sunrise		
7 Feb 2007	67.9	21.0	n/a	34	Ascent[a]	Esrange	Sweden
22 Feb 2007	67.9	21.1	25	34	Ascent[a]	Esrange	Sweden
22 Sep 2007	35.2	−114.1	10	38	Sunset	Ft. Sumner	New Mexico
23 Sep 2007	34.0	−110.3	13	38	Sunrise		
23 Sep 2011	34.5	−108.8	6	39	Sunset	Ft. Sumner	New Mexico
24 Sep 2011	35.7	−96.3	14	40	Sunrise		
13 Sep 2014	36.2	−112.5	7	39	Sunset	Ft. Sumner	New Mexico
14 Sep 2014	35.6	−103.5	8	40	Sunrise		
27 Sep 2016	36.0	−110.5	11	39	Sunset	Ft. Sumner	New Mexico

n/a – not applicable.

Table 2. Attributes of the five spectral windows used to fit OCS in MkIV balloon spectra. Center and Width denote the center wavenumber and width of the window. OCS band denotes the vibration–rotation state to which the OCS molecules were excited. The Retrieved VMR scale factor shows how the average OCS amounts retrieved from a particular window compare with the mean of all windows. S_{MAX} is the maximum line intensity in units of cm^{-1} (molec. $cm^{-2})^{-1}$. The windows centered at 2050 and 2070 cm^{-1} cover the P- and R-branches of the strong ν_3 band, and therefore allow accurate estimation of OCS amounts at the higher altitudes. The three weaker windows (868, 2916, and 4096 cm^{-1}) have larger biases and uncertainties, but are collectively consistent with the two strong ν_3 windows.

Center (cm^{-1})	Width (cm^{-1})	OCS band	Interfering gases fitted	Retrieved VMR scale factor	S_{MAX}
868.05	11.3	ν_1	hno3 h2o co2	1.115 ± 0.097	1.54×10^{-20}
2050.20	24.2	ν_3	co2 o3 h2o co	0.996 ± 0.012	1.18×10^{-18}
2069.65	12.7	ν_3	co2 o3 h2o co	0.996 ± 0.019	1.25×10^{-18}
2915.55	38.0	$\nu_1 + \nu_3$	ch4 o3 h2o hcl no2 c2h6 hdo	0.80 ± 0.23	1.53×10^{-20}
4096.00	39.8	$2\nu_3$	ch4 h2o hdo hf	0.95 ± 0.24	8.26×10^{-21}

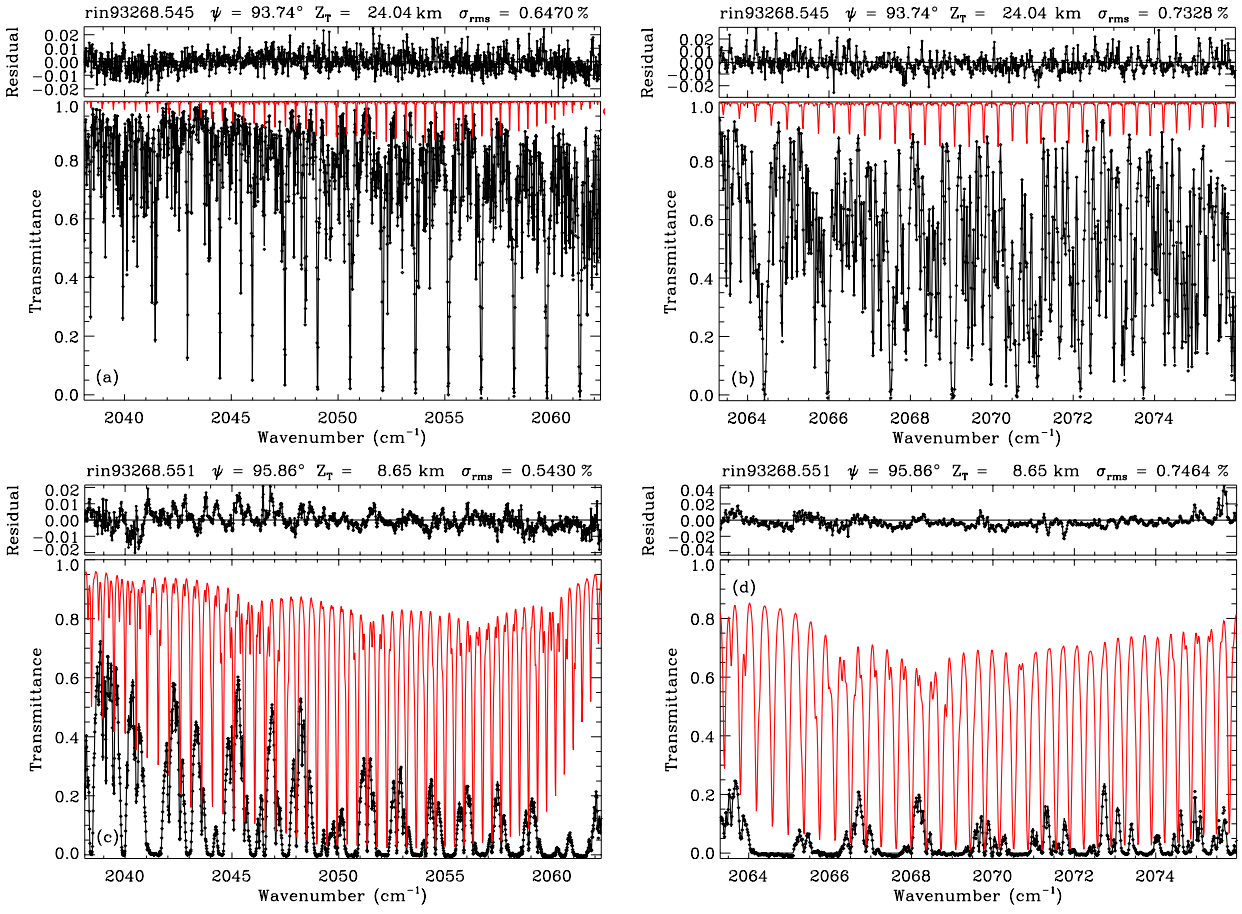

Figure 1. Examples of spectral fits to MkIV balloon spectra measured at 24.0 km **(a, b)** and 8.7 km **(c, d)** tangent altitude. Panels **(a, c)** show fits to the *P*-branch. Panels **(b, d)** show fits to the *R*-branch. Black points represent the measured spectra. The black line is the fitted calculation. The red line shows the OCS contribution to the fitted calculation. Interfering gases are primarily CO_2, H_2O, and O_3. Figure S1 in the Supplement shows the same fits but with an expanded x-scale and with the individual interfering gases shown in different colors.

H_2O, and CO absorption), as can be seen in the lower panels of Fig. 1.

Three additional windows, centered at 868, 2916, and 4096 cm^{-1}, containing much weaker OCS absorption bands are therefore used to provide additional information at lower altitudes, and to provide a cross-check on the absolute OCS values retrieved in the ν_3 band. It is important that the strong and weak windows are consistent in terms of the retrieved OCS amounts, or else the retrieved vmr profiles will be skewed, with the ν_3 band dominating above 10 km altitude, and the weaker bands contributing below.

Collectively, the three weak windows have an average VMR scale factor close to 1.0, and therefore will not skew the retrieved vmr profiles when results from the five windows are combined. Since the balloon spectra are ratioed (limb spectra divided by a high-sun spectrum), only two or three continuum basis functions are used, even for the widest windows, and no solar spectrum is needed.

The 41 N_2O windows used in the analysis of MkV balloon spectra are listed at http://mark4sun.jpl.nasa.gov/m4data.html. These cover the 1183 to 4750 cm^{-1} spectral regions with widths up to 50 cm^{-1}. These include weak lines to accurately retrieve tropospheric N_2O, and strong lines for upper stratospheric N_2O.

2.4 Balloon results

Figure 2a shows 26 OCS profiles plotted versus altitude and color-coded by year (blue: 1990; green: 2000; red: 2015). The green points, measured in 1997–2003 at high latitudes, have lower OCS amounts than the other flights. This is due to stratospheric descent at high latitude, especially in the winter. Figure 2b shows the same data but color-coded by latitude (blue: 35° N; red: 67° N). The profiles measured at high latitude (Fairbanks in 1997; Esrange in 1999–2003) have much lower stratospheric OCS than the mid-latitude flights made prior and later.

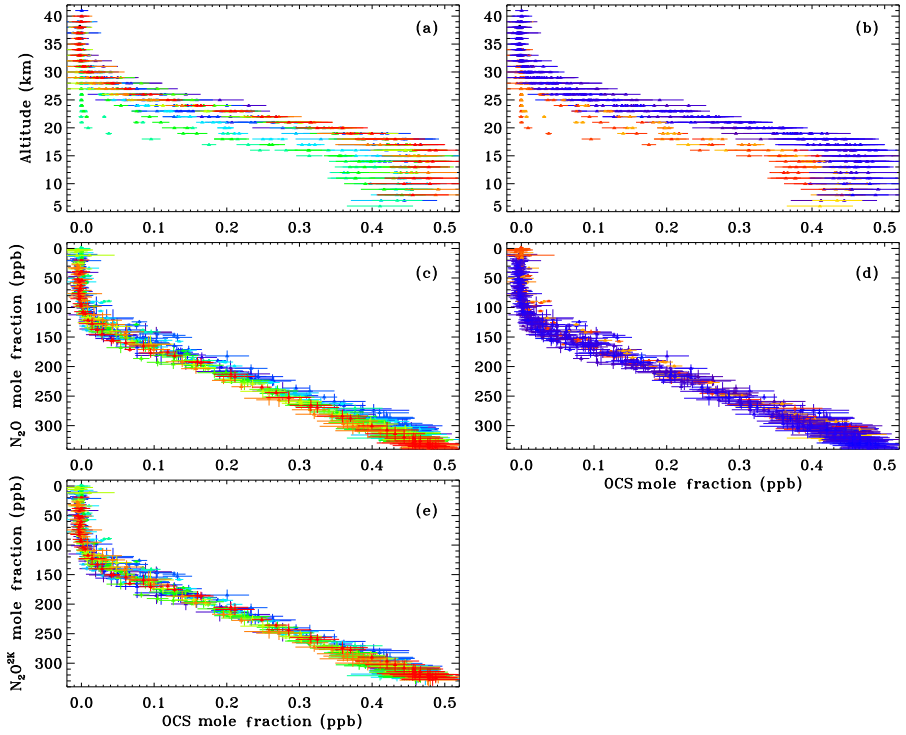

Figure 2. Profiles of OCS retrieved from MkIV balloon spectra by averaging results obtained from the five windows listed in Table 1. In the left-hand panels the points are color-coded by year (e.g., blue: 1990; green: 2000; red: 2014). In the right hand panels the same data are color-coded by latitude (blue: 35° N; red: 67° N). In the top panels **(a, b)**, the OCS is plotted versus altitude. In the middle panels **(c, d)**, the OCS is plotted versus N_2O. In the bottom panel **(e)** the N_2O has been de-trended by 0.25 % yr^{-1} such that it represents the year 2000 (N_2O^{2K}). Only data with OCS uncertainties <50 ppt and N_2O uncertainties < 20 ppb were plotted, which reduced the total number of points in each panel from 756 to 668.

Fortunately, the effects of transport, and their variations with latitude and season, can largely be removed by using N_2O as the vertical ordinate, as seen in panels (c) and (d). This results in a much tighter consistency between the various profiles. Figure 2c shows that in the later years (red) there is more N_2O at a given OCS value than in the early years (blue). Conversely, there is less OCS at a given N_2O level. This implies an increasing trend in N_2O or a decreasing trend in OCS, or both. Figure 2d reveals that the OCS–N_2O relationship is virtually independent of the measurement latitude, to within the scope and precision of these measurements. Incidentally, Fig. 2d shows that despite the mid-latitude balloon flights (blue) reaching higher altitudes (40 km) than the polar flights (red; 30–34 km), N_2O never falls below 15 ppb at mid-latitudes, whereas at high latitudes it falls to zero. This is a consequence of downward transport in the stratosphere at high latitudes.

Figure 2e shows the same data as in panel (c), but with the N_2O values adjusted for the known 0.25 % yr^{-1} increase seen in in situ measurements. Over the timespan of the MkIV measurements, N_2O has increased from 307.5 ppb in 1989 to 326.7 ppb in 2014, according to accurate in situ measurements (e.g., https://www.eea.europa.eu/data-and-maps/daviz/atmospheric-concentration-of-carbon-dioxide-2#tab-chart_4), which represents 6.24 % in 25 years or 0.25 % yr^{-1}. A similar rate of increase is to be expected in the stratosphere. It is fortunate that the increase has been so linear because this makes it independent of the age of the air, and hence altitude, simplifying the implementation of a correction.

Correcting the measured N_2O to its 2000 value eliminates the time-dependent creep in the OCS–N_2O relationship seen in Fig. 2c, resulting in a further tightening of their correlation. The OCS–N_2O^{2K} relationship plotted in Fig. 2e is highly linear (Pearson correlation coefficient of 0.982) for N_2O^{2K} values down to 119 ppb, which represents ∼ 10 mbar pressure or ∼ 30 km at mid-altitudes. At higher altitudes the OCS goes to zero before N_2O, reflecting the shorter stratospheric lifetime of OCS. This causes a "knee" in the OCS–N_2O relationship, such that the overall relationship can be reasonably approximated by the equations

$$\begin{aligned} \mathrm{OCS} &= 2.25\times10^{-3}(\mathrm{N_2O^{2K}} - 119\,\mathrm{ppb}) && \mathrm{N_2O^{2K}} > 119\,\mathrm{ppb},\\ \mathrm{OCS} &= 0 && \mathrm{N_2O^{2K}} < 119\,\mathrm{ppb}. \end{aligned}$$

This relationship will later be used in the analysis of ground-based measurements.

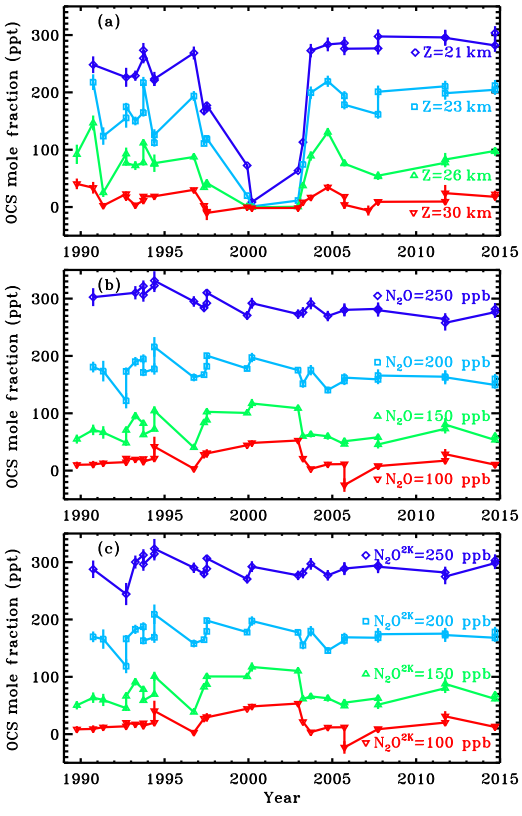

Figure 3. **(a)** Stratospheric OCS dry mole fractions interpolated onto four different altitudes (21, 23, 26, and 30 km) using the data from Fig. 1. **(b)** The same OCS data interpolated to various N_2O isopleths. The 250 ppb isopleth (red) corresponds to $\sim$21 km altitude at mid-latitudes, whereas the 100 ppb isopleth (blue) corresponds to $\sim$30 km. **(c)** Same as **(b)**, but with the N_2O amounts detrended by 0.25 % yr^{-1}, as in Fig. 2e.

Figure 3 shows the same OCS and N_2O balloon data that were presented earlier in Fig. 2, but the OCS has been interpolated onto fixed altitudes and N_2O isopleths. In Fig. 3a, the small OCS amounts from 1997 to 2002 were due to the balloon flights being undertaken at high latitudes. Examined this way, these OCS data are clearly not useful for determining trend information. In Fig. 3b, the same OCS data are interpolated onto various N_2O isopleths. This removes transport-driven variations in the amounts of stratospheric OCS due to latitude or seasonal differences between flights, since these are common to OCS and N_2O. The resulting OCS appears to be decreasing with time at the lower altitudes (larger N_2O isopleths), but this is an artifact of the increase in atmospheric N_2O: the isopleths get higher in altitude over time, which results in the appearance of a decreasing trend in an unchanging gas such as OCS. Figure 3c shows the same data as panel (b), but with the N_2O isopleths corrected to their values in the year 2000 under the assumption of a +0.25 % yr^{-1} trend. This eliminates artifacts due to the secular increase in N_2O, while still preserving its ability to remove dynamically induced fluctuations from the OCS record. Figure 3c shows no significant trend in stratospheric OCS at any level. Based on this, we conclude that stratospheric OCS has not changed by more than 5 % over the past 25 years.

2.5 Ground-based observations

The MkIV instrument has also made ground-based observations since 1985 from a dozen different sites. These measurements were taken with the same instrument and processed with the same software (phase correction, FFT, spectral fitting retrieval) and spectroscopic linelists as the balloon observations to provide the best possible internal consistency of results. Table 3 lists these ground-based sites, their locations, and the number of observations (N_{obs}) and observation days (N_{day}) from each. The majority of the data come from the JPL (0.35 km) and Mt. Barcroft (3.80 km), both in California. On a typical day we might take 30 spectra at 120 cm maximum optical path difference over a period of 1.5 h. After discarding bad spectra (e.g., when clouds blocked the sun), the remainder are averaged into forward–reverse pairs at high solar zenith angles when the air mass is changing rapidly, or in fours or sixes at lower zenith angles when the air mass is changing slowly. The net result is a few average spectra per day. We then use the GFIT algorithm to retrieve vertical column abundances from these average spectra. Over 30 different gases are retrieved, including OCS and N_2O. These results can be found at http://mark4sun.jpl.nasa.gov/ground.html.

We do not attempt to fit the whole spectrum. Instead we seek spectral regions in which the absorption lines of the gases of interest (i.e., OCS, N_2O) are strong (but not saturated), reasonably temperature-insensitive, and not overlapped by large residuals originating from interfering gases (e.g., H_2O, CO, CO_2). Initially, 21 candidate OCS windows were defined and analyzed in ground-based spectra, all from the strong ν_3 band (see Table B1 in Appendix B). None of the weaker OCS bands (at 868, 2915, and 4096 cm^{-1}) were used in the analysis of ground-based spectra: their OCS absorptions are simply too weak and overlapped with interfering absorptions. Most of these 21 windows were taken from previous publications on ground-based OCS measurements: Griffith et al. (1998), Rinsland et al. (2002), Krysztofiak et al. (2015), Kremser et al. (2015), and Lejeune et al. (2017). In addition, four new, much-broader windows were also evaluated, in which most of the OCS lines are overlapped by stronger interfering absorbers. This would bar them in the traditional Detection of Atmospheric Composition Change (NDACC) window selection process, which avoided strong interferences. In the present work, however, the presence of an interfering absorption line overlapping the OCS line of interest is not necessarily a disqualification, unless it produces a large residual.

To avoid a major digression, the details of the OCS window selection process are relegated to Appendix B. Suffice

Table 3. MkIV ground-based observation sites, their locations and altitudes, and the number of observations and observation days from each site as of the end of 2016, sorted by latitude. N_{obs} is the number of observations. N_{day} is the number of observation days.

Town	State	N_{obs}	N_{day}	Latitude (deg.)	Longitude (deg.)	Altitude (km)
Esrange	Sweden	160	32	67.889	+21.085	0.271
Fairbanks	Alaska	124	46	64.830	−147.614	0.182
Manitoba	Canada	20	5	56.858	−101.066	0.354
Mt. Barcroft	California	1369	255	37.584	−118.235	3.801
Mtn View	California	7	4	37.430	−122.080	0.010
Daggett	California	33	21	34.856	−116.790	0.626
Ft. Sumner	New Mexico	216	71	34.480	−104.220	1.260
Wrightwood	California	475	45	34.382	−117.678	2.257
JPL (B183)	California	1709	577	34.199	−118.174	0.345
JPL (mesa)	California	20	5	34.205	−118.171	0.460
Palestine	Texas	4	3	31.780	−95.700	0.100
McMurdo	Antarctica	37	20	−77.847	+166.728	0.100

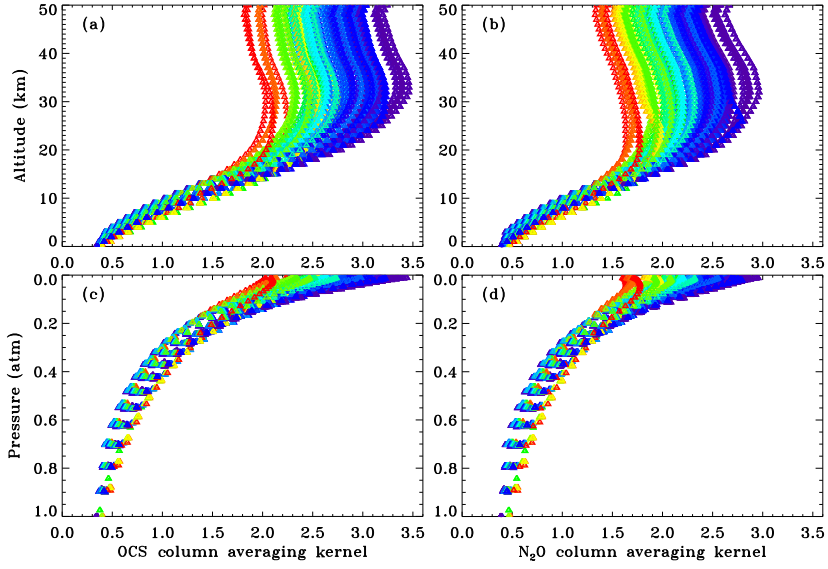

Figure 4. Ground-based column averaging kernels plotted versus altitude **(a, b)** and pressure **(c, d)**. Panels **(a, c)** show OCS kernels. Panels **(b, d)** show N_2O kernels. Values are color-coded by air mass (purple: 1; green: 3; red: 10). A representative sub-set of 135 different observations, representing different sites and conditions, was used to make this plot. The fact that the OCS and N_2O kernels are similar in shape is not a fortuitous accident. The N_2O windows used in this study were selected to contain weak N_2O lines only, matching the OCS lines in terms of line depth and hence kernel shape. Since the shapes of the OCS and N_2O kernels are similar, so will be their sensitivity to stratospheric transport.

it to state here that just two OCS windows were eventually chosen for subsequent use: a 13 cm^{-1} wide window centered at 2051.3 cm^{-1} containing 28 *P*-branch lines of OCS, and a 9 cm^{-1} wide window centered at 2071.1 cm^{-1} containing 26 *R*-branch lines. OCS amounts presented subsequently are the result of averaging these two windows.

A similar spectral fitting analysis was performed for N_2O. Since the tropospheric variations in N_2O are small, the column variations are controlled mainly by stratospheric transport. This allows the retrieved N_2O amounts to be used to compensate for variations in the column OCS arising from stratospheric transport. Wang et al. (2014) used N_2O in this manner to remove stratospheric variations from column CH_4. The detailed discussion of the N_2O window selection is relegated to Appendix C to avoid a major detour here. Suffice it to say that a subset of N_2O windows was selected based on three criteria: (1) high precision, (2) consistency in the retrieved N_2O amounts, and (3) averaging kernels similar to those of OCS. The latter criterion was achieved by choosing windows with N_2O absorption depths similar to those of OCS, and discarding windows with strong N_2O lines. Figure 4 compares averaging kernels for OCS and N_2O. Their

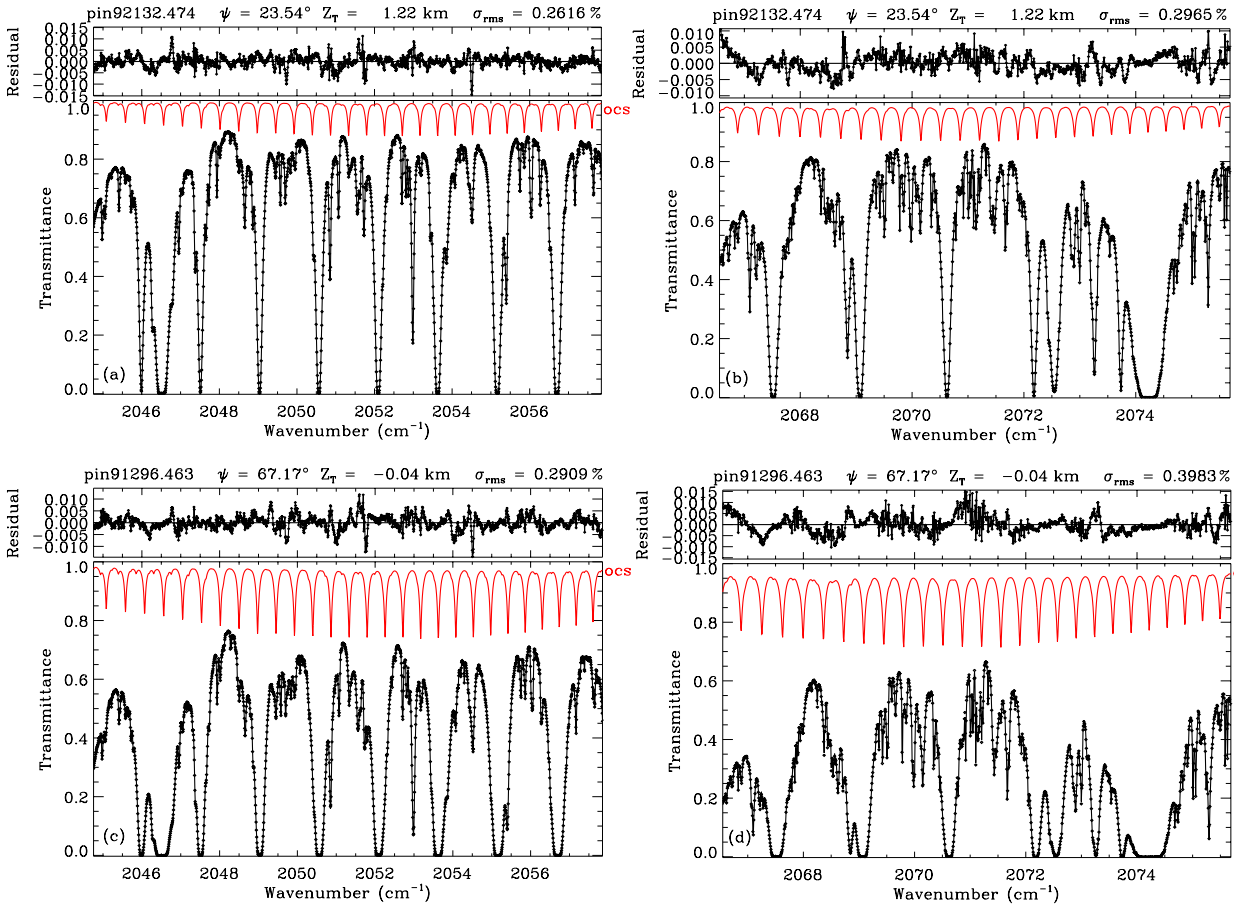

Figure 5. Examples of spectral fits to ground-based MkIV spectra. Panels **a, c)** show fits with the 2051 cm^{-1} window covering most of the P-branch of the ν_3 band. Panels **(b, d)** show fits to the 2071 cm^{-1} window covering the center of the R-branch. Panels **(a, b)** show fits to a low-air-mass (SZA = 24°) spectrum. Panels **(c, d)** show fits to a higher air-mass spectrum (SZA = 67°). Black symbols show the measured spectrum, and the black line is the fitted calculation. The red line is the OCS contribution to the fitted calculation. The individual contributions of other gases (mainly H_2O, CO_2, CO, O_3) are not shown because they would clutter the figure, obscuring the OCS. The saturated lines with a spacing of 1.6 cm^{-1} are CO_2. Despite CO_2 being the strongest absorber, the residuals (measured–calculated) shown at the top of each panel are dominated by H_2O and CO interferences.

closely matching shapes means that information about atmospheric OCS and N_2O has a similar altitude distribution and is therefore directly comparable.

Figure 5 shows examples of fits to ground-based MkIV spectra in the two selected windows. The left panels show fits over the 2051 cm^{-1} window covering 28 of the strongest P-branch lines of the ν_3 band. The right panels show fits to the 2071 cm^{-1} window covering 26 strong OCS lines in the center of the R-branch. The upper panels show fits to a low-air-mass (SZA = 23°) spectrum and the lower panels to a higher-air-mass spectrum (SZA = 67°). Although the OCS lines are stronger in the high-air-mass spectrum, so are the interfering absorptions. This tends to decrease the precision and accuracy of the OCS retrievals as zenith angle increases.

2.6 Ground-based results

Figure 6a and b show OCS column amounts retrieved from spectral fits such as those shown in Fig. 5. The points are color-coded by the logarithm of site altitude (blue: 0 km; red: 3.8 km). The same data are plotted in both panels, on the left versus year and on the right versus day of year. The high-altitude observations (red) clearly show substantially less column OCS. Figure 6c and d show xOCS: the OCS column divided by the dry air column, the latter obtained by subtracting the H_2O column from the total column of all gases, which is inferred from the measured surface pressure. This division improves the consistency of xOCS values retrieved from different altitude sites, but there is still a ∼ 15 % spread, which makes it difficult to quantify the long-term trends and the seasonal cycle. Figure 6e and f show the OCS / N_2O col-

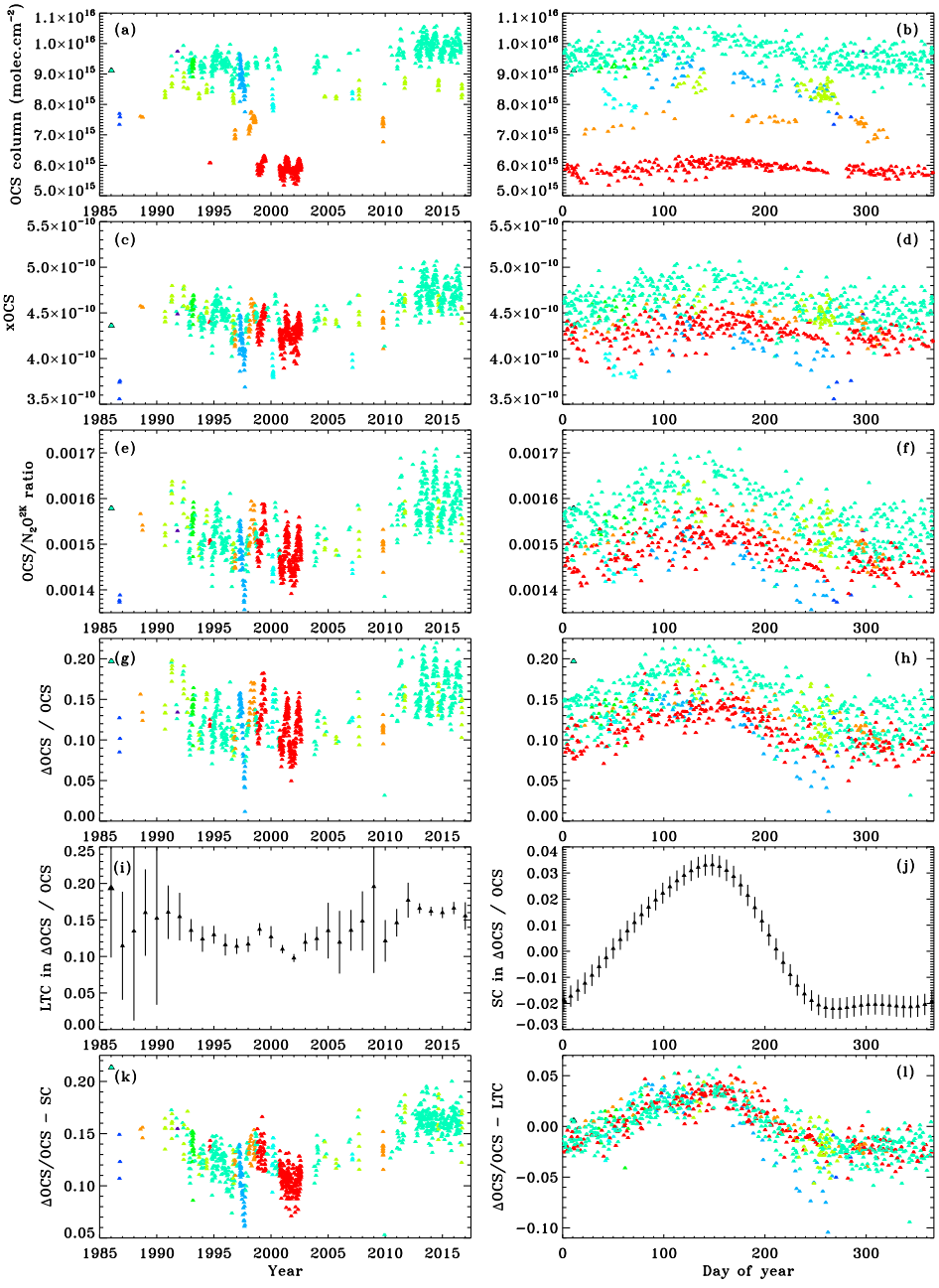

Figure 6. Ground-based measurements of OCS, color-coded by site altitude (e.g., dark blue: 0 km; light blue: 0.1 km; green: 0.3 km; lime: 1.2 km; orange: 2.1 km; red: 3.8 km). The left-hand panels show the OCS plotted versus year, revealing the long-term changes (LTC). The right-hand panels show the same data plotted versus the day of the year, revealing the seasonal cycle (SC). Panels **(a, b)** show the raw column abundances, which are much larger at the lower-altitude sites. Panels **(c, d)** show the column-averaged OCS amounts (xOCS), which reduces the altitude and site dependence. Panels **(e, f)** show the OCS / N_2O column ratios, which further reduce the altitude–site dependence. Panels **(g, h)** show ΔOCS, the difference between the measured OCS, and the N_2O-based prediction described in Appendix A. Subtracting the N_2O-derived OCS amount eliminates dynamically induced variations common to both gases, revealing the tropospheric behavior with more fidelity. Panels **(i, j)** show the LTC and the SC extracted from the ΔOCS results by simultaneously fitting a linear spline and harmonic terms. Panel **(k)** shows the ΔOCS data with the SC subtracted. Panel **(l)** shows the SC with the LTC subtracted. For right-hand panels without *y*-axis labels **(b, d, f, h)**, the left-hand panel labels are valid.

umn ratio. We know from the balloon measurements that OCS and N_2O have similarly shaped vmr profiles (at least up to 30 km) and are both subject to the same dynamical perturbations; therefore dividing the OCS by N_2O cancels most of the transport-driven variations. Thus the OCS / N_2O column ratio is less variable than the xOCS, with a $\sim 10\,\%$ spread of values, despite the N_2O bringing noise into the ratio. However, since the OCS–N_2O relationship seen in the balloon data does not go linearly through the origin, the effects of stratospheric transport are greater on OCS than N_2O and therefore do not completely cancel when taking the ratio.

To more completely remove stratospheric transport effects from the OCS measurements, we exploited the relationship established in Fig. 2e using MkIV balloon measurements. Appendix A details how, under the assumption that the changes in N_2O are entirely stratospheric in origin, the N_2O column may be used to remove stratospheric transport effects from the OCS column measurements. Figure 6g and h show the resulting ΔOCS as defined by Eq. (A3). This results in a slightly improved consistency between measurements made at different sites and a more compact seasonal cycle, as compared with Fig. 6e and f. The long-term changes (LTC) of OCS are unfortunately still obscured by the seasonal cycle, which is roughly the same amplitude. Similarly, the seasonal cycle of OCS is obscured by the LTC. Due to the irregular sampling of the observations, the seasonal cycle cannot simply be averaged out by smoothing the observations. For example, in some years we take data in Ft. Sumner, New Mexico, in September only, near the minimum of the OCS seasonal cycle. This would drag down the mean for those years, if the seasonal cycle were not accounted for.

We therefore simultaneously fitted a linear spline and harmonic terms through the OCS data in Fig. 6g and h. The resulting function is continuous with respect to time. The seasonal cycle is fitted as independent sine and cosine terms with 12-, 6-, and 4-month periods (i.e., the first three harmonics), requiring six unknown parameters in total. The choice of three harmonics reflects the improved fit to the data as compared with two harmonics, and the lack of improvement using four harmonics. This parameterization assumes the seasonal variation is assumed to be identical each year and independent of the site (altitude or latitude).

The spline fitted to the LTC had "knots" at the beginning of each year, requiring 33 of these to cover 1985 to 2017. Between knots, the spline was assumed to be linear with time. The resulting matrix equation is linear in the $33 + 6 = 39$ unknown parameters, so no iteration is required. In this way, 39 pieces of information are extracted from the 683 OCS measurements.

The use of a spline to represent the long-term changes has the advantage that an outlier in one particular year only affects the knots that bracket it. This is in contrast to fitting a polynomial (i.e., $y = a + bt + ct^2 + dt^3 + \ldots$) which would allow an anomalous point at one end of the time series to impact the fitted curve everywhere, even at the other end. Figure 6i and j show the LTC and the seasonal cycle (SC) extracted in this manner from the ΔOCS data. Figure 6i shows the spline values at the yearly knots, along with their uncertainties. In years with little or no data (e.g., 1990, 2009) the spline values have large uncertainties. Also, in years when the de-seasonalized xOCS amounts deviate from a straight line, uncertainties will be large. The results show a 5 % drop (from 0.13 to 0.08) over the 1990 to 2002 period, followed by a 5 % increase from 2002 to 2012. Since 2012, ΔOCS has been flat.

We note that the anomalously low data points in October 1986 were measured from McMurdo, Antarctica. Since OCS was measured to be $10 \pm 4\,\%$ larger in the Arctic than the Antarctic (Notholt et al., 1997), the McMurdo measurements have much lower values than the other points around that time, which were all in the Northern Hemisphere. These McMurdo points drag down the spline value at the 1987.0 knot in Fig. 6i.

Figure 6j shows the seasonal component extracted from the ΔOCS data, plotted at weekly intervals. It shows a steady increase in OCS during winter and spring with a maximum around day 145, followed by a rapid decrease in summer with the maximum loss rate at day 200. There is little change in the autumn. The peak-to-peak amplitude is 5–6 % of the total OCS column. This is more than double the $2.56 \pm 0.80\,\%$ peak-to-peak seen by Rinsland et al. (2002) from Kitt Peak, at a similar latitude to the majority of the MkIV data, and at an altitude within the range of the MkIV observations. The inferred MkIV seasonal cycle is consistent with Wang et al. (2016) who reported xOCS data from five Network for the NDACC sites over the period 2005–2013. As expected, the amplitude of the MkIV seasonal cycle, which is representative of $\sim 35°$ N, is intermediate in value between that from the Jungfraujoch at 46° N (10–12 % peak-to-peak) and Mauna Loa at 20° N (4–5 %).

Figure 6k shows the ΔOCS data with the seasonal cycle subtracted. This makes the LTC clearer. Figure 6l shows the ΔOCS data with the LTC subtracted, which greatly improves the compactness of the seasonal behavior. For example, the fact that the minimum OCS occurred in 2002, when the MkIV was taking measurements from 3.8 km altitude (red points), caused the red points to be systematically low in Fig. 6h, but this discrepancy disappears in Fig. 6l with the removal of the long-term changes.

The greater fidelity of the data in Fig. 6l reveals some outliers. The blue data points, measured from Fairbanks, Alaska, during the summer of 1997 (the only time we were there) show a much larger drawdown of ΔOCS than is captured by the average seasonal cycle, which is representative of 35° N. This may be related to the location of Fairbanks within the boreal forest, whose rapid summertime growth absorbs CO_2 and OCS from the atmosphere. Aside from this, there is remarkable consistency between the other sites, despite their huge range of altitudes.

Table 4. Error budget of retrieved ground-based OCS amounts. The precision is the likely difference between observations made under nominally identical conditions. It is smaller than the absolute accuracy due to the absence of stationary errors, which are the same or similar in every observation.

Error type	Absolute accuracy (%)	Precision (%)
Spectroscopy		
OCS intensities	5	0
OCS air-broadening	5	2
Interfering gases	4	2
Interfering solar	2	0
ILS	2	1
Spectrum errors		
Zero level offsets	2	1
Phase errors	2	2
Channel fringes	2	1
Ghosts	1	1
Forward model	1	0
Smoothing error		
OCS	5	2
Interferers	5	2
T/P profile	4	3
Measurement noise	1	1
RSS total	12	6

2.7 Error budget (ground-based)

It is not straightforward to categorize all errors in terms of random or systematic. While the contribution of measurement noise is clearly 100 % random, and that of line intensities is 100 % systematic, most error sources have hybrid characteristics. That is, over a sufficiently short timescale they can be considered invariant, but over longer time periods they become more random. For example, atmospheric temperature errors can be considered a fixed systematic error over a period of minutes, but their effect on measurements made hours and days apart is much more random. Table 4 attempts to quantify the uncertainties resulting from various error terms. In terms of the absolute accuracy of the measurements, all error terms contribute fully. In terms of the precision, invariant errors (e.g., line intensities) do not contribute at all and the hybrid terms contribute partially.

Regarding the integrity of the seasonal cycle shown in Fig. 6j, the largest risk is site-to-site differences, coupled with the fact that measurements from certain sites (e.g., Ft. Sumner) only happen at particular times of the year (September). For example, if the Ft. Sumner xOCS were biased low, then this would exaggerate the seasonal cycle because September happens to be the minimum of the seasonal cycle. But the fact that the de-trended data in Fig. 6l show good site-to-site consistency (apart from Fairbanks, Alaska) reduces the possibility of a large site-to-site bias.

Of course, although invariant systematic errors (e.g., spectroscopic line intensities) drive up the absolute uncertainty, they do not degrade our ability to determine trends. Spectroscopic line widths, on the other hand, can change the derived trend due to the altitudes of the various sites, and hence the pressure broadening. After consideration of the use of N_2O to reduce the effects of smoothing error from 5 to 2 %, we estimate that the precision of these MkIV OCS measurements is 6 %. With many years of data with this precision, OCS changes as small as 3 % can be detected in MkIV ground-based data.

3 Discussion

Various groups have reported changes (or lack thereof) in atmospheric OCS over the past 2 decades. Griffith et al. (1998) reported "seasonal cycles in the OCS total columns from both Lauder and Wollongong with peak-peak (p-p) amplitudes of 6 and 18 %, respectively, with both cycles peaking in late summer (mid-February). An apparent cycle amplitude of about 5 % is expected as a result of tropopause height variations, and the remainder can be ascribed to seasonal cycles in tropospheric mixing ratios. The secular trend in OCS was < 1 %/year". This implies that the 5 % seasonal cycle seen at Lauder was mainly due to tropopause height variations and that the actual variation in tropospheric OCS mole fraction was only 1 % at Lauder and 13 % at Wollongong.

In our analysis, the OCS variation due to tropopause height variation has already been implicitly removed from the ΔOCS by the N_2O correction, since the tropopause height variations also influence N_2O. This being the case, our 5–6 % seasonal variation can be considered intermediate between the Lauder (1 %) and Wollongong (13 %) values.

Rinsland et al. (2002) reported a trend of $-0.25 \pm 0.04\,\%\,\mathrm{yr}^{-1}$ in the OCS column below 10 km above Kitt Peak over the period 1978 to 2002 with a seasonal cycle of 1.28 ± 0.40 % amplitude. This was based on fitting a straight line to the long-term trend and a two-coefficient seasonal cycle with a 1-year period.

Kremser et al. (2015) report OCS increases of $0.5\,\%\,\mathrm{yr}^{-1}$ from three Southern Hemisphere sites (34, 45, 78° S) over the period 2001–2014. They used a linear spline with user-selected knot points to represent the long-term behavior, after removing the seasonal variation. Lejeune et al. (2017) reported a $4\,\%\,\mathrm{yr}^{-1}$ increase in the OCS partial column from 13.8 to 19.5 km over the period 1995–2015. For the tropospheric partial column (3.6–8.9 km), a 6 % drop from 1995 to mid-2002 was reported, then a 7 % increase to 2008, and it has been constant since then. This behavior is highly consistent with the behavior seen in the MkIV ground-based dataset.

Figure 7 shows the long-term secular changes and seasonal cycle of xCO_2, derived from the same MkIV ground-based spectra using 20 CO_2 windows covering the 2480 to $4924\,\mathrm{cm}^{-1}$ region. The xCO_2 underwent a similar analysis to that performed for OCS in Fig. 6i and j, with the exception that the N_2O correction was not performed because it

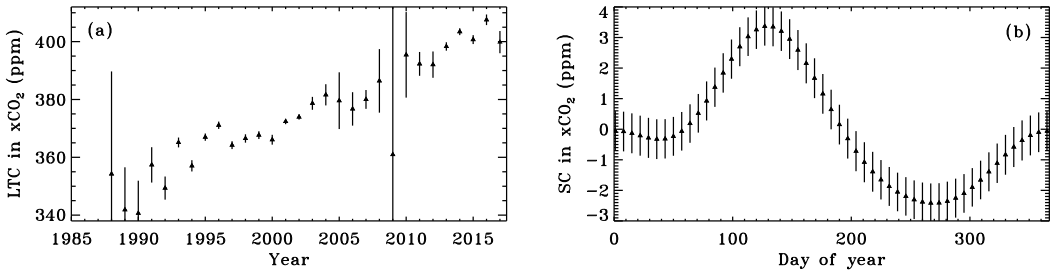

Figure 7. Decomposition of MkIV ground-based measurements of xCO_2 into a long-term secular trend **(a)** and a seasonal cycle **(b)**. Years with little data, or with inconsistent xCO_2 values, have large uncertainties. The seasonal cycle has its peak around day 130 and its maximum rate of decrease around day 185.

would likely do more harm than good, given that the CO_2 profile decreases by only $\sim 2\,\%$ in the stratosphere (versus $100\,\%$ for OCS). Hence the N_2O-related errors introduced would likely have been larger than that of the transport errors removed. The resulting xCO_2 seasonal cycle obtained is 5–6 ppm (1.4 %) in peak-to-peak amplitude and has a similar shape to that of xOCS in Fig. 6j. This similarity is consistent with OCS being absorbed by plants during photosynthesis. Upon closer inspection of Fig. 7, the xCO_2 peak occurs around day 130 and the fastest xCO_2 loss occurs around day 185. These are each about 2 weeks earlier than for xOCS.

The use of N_2O to reduce the effects of stratospheric transport on OCS relies on the fact that stratospheric transport affects both gases similarly. In terms of the ground-based measurements, N_2O has the advantage over other tracers (e.g., CH_4) that its tropospheric dry mole fraction is very stable with a seasonal variation of $< 0.1\,\%$. Thus we can unambiguously attribute larger variations in xN_2O at a particular site to the stratosphere. Moreover, N_2O can be measured to a high precision over a wide range of measurement conditions.

The MkIV balloon measurements show no significant trend at the $N_2O^{2K} = 250$ ppb isopleth (see Fig. 3c), which corresponds to ~ 21 km altitude at mid-latitudes, or at any other level. Over the 1995–2015 period, the change in MkIV OCS was $-1 \pm 3\,\%$, as compared with $4 \pm 1\,\%$ from Lejeune et al. (2017). These estimates do not quite overlap, but given that the altitudes and latitudes are different, the small discrepancy is not a cause for concern.

Historically, atmospheric trace gas abundances were retrieved using narrow windows centered on isolated absorption lines of the gas of interest. This was computationally fast and avoided the worst interferences. From the ν_3 OCS band, just 2 or 3 of the cleanest OCS lines were typically utilized. Faster computers now make it possible to fit far wider windows containing many more OCS lines, promising improved precision. The question is: does this improve the OCS retrieval? The answer depends on the quality of the radiative transfer calculation, including the atmospheric T/P/Z and VMR profiles, and the spectroscopy, in particular that of the interfering lines. For example, including an OCS line overlapped by a T-sensitive H_2O line will make the retrieval sensitive to lower tropospheric temperature errors. But if the temperature model is accurate, then adding the overlapped OCS line will nevertheless improve the retrieval.

Besides improving precision due to utilization of more target lines, wide windows have other benefits. Retrievals are more robust than from narrow windows in the sense that you are less likely to get a good fit (and hence a small uncertainty) for the wrong reasons, and the likelihood of non-convergence is reduced. Regions blacked out by CO_2 and H_2O lines, although containing no information about the target gas, allow correction of zero offsets, which affect stronger interfering gases, which in turn affect the target gas retrievals. While the direct effect of zero offset on a weakly absorbing target gas is small, the indirect effect can be much larger. Broad windows also facilitate the identification and correction of channel fringes, although this was not necessary in the OCS windows in the MkIV spectra. Broad windows also allow a more accurate estimate of the Doppler shift of the solar Fraunhofer lines, of which there are many (arising from solar CO) in the 2000–2100 cm^{-1} region. These Doppler shifts cannot be accurately calculated since a large component arises from mispointing of the solar tracker.

We are not claiming that broad windows are always better than multiple narrow windows. It depends on how well the overlapping interferences can be accounted for. This must be decided on a case-by-case basis and will depend on the quality of the spectroscopy and the a priori T/P/VMR profiles. The altitude of the observation site(s) can also be important, especially for windows containing H_2O absorptions.

4 Summary and conclusions

We have retrieved OCS from over 30 years of MkIV balloon and ground-based spectra. Simultaneous measurements of N_2O were used to reduce the effects of stratospheric transport on the OCS amounts, yielding better information on the tropospheric trends and seasonal cycle. This makes no assumptions about the tropopause altitude or the stratospheric profile of OCS (other than its relationship with N_2O). Bal-

loon results yield no significant stratospheric trend. Tropospheric OCS, on the other hand, shows a 5 % decrease during 1990–2002, followed by a 5 % increase from 2003 to 2012. There was no discernible change since 2012. The reasons for this behavior are not fully understood. Lejeune et al. (2017) speculate that this dip is partly due to a reduction in industrial OCS-forming emissions in the 1990s.

We have also derived a tropospheric seasonal cycle which is 5–6 % of the total column at 35° N and much larger at 65° N, the latter based on 1997 measurements from Fairbanks, Alaska. The OCS seasonal cycle is similar in shape to that of CO_2, implying uptake by plants during photosynthesis, but is 4–5 times larger, expressed as a fraction of the total column.

The fact that the balloon and ground-based measurements were taken with the same instrument and analyzed with the same software (phase correction, FFT, spectral fitting) and spectroscopic linelists provides the best possible internal consistency of results.

This work also highlights the advantages of using wide windows containing 20–30 lines of the target gas, versus the traditional NDACC strategy of using 2–3 narrow windows, each containing a single well-isolated target line. Despite the root mean square (RMS) spectral fits being typically a factor 2 worse for the wide windows (due to interfering absorptions), the precisions of the retrieved target gases are generally superior than for narrow, single-line windows. This is mainly because the increased number of target lines outweighs the degradation of the spectral fits. Also, the presence of saturated interfering lines allows an accurate retrieval of any zero level offset. The wide windows allow a better characterization of any channel fringes in the spectra and solar Doppler shifts.

In the future, as we improve our ability to model atmospheric radiative transfer (i.e., spectroscopic parameters, atmospheric P/T analyses), we can anticipate the systematic residuals decreasing, allowing the broad windows to perform even better. In contrast, the narrow windows, already being fitted close to the spectral noise level, will not improve as much.

Data availability. The column abundances used in this study can be downloaded from https://mark4sun.jpl.nasa.gov/ground.html.

These data are also available from the NDACC archive: ftp://ftp.cpc.ncep.noaa.gov/ndacc/station/barcroft/ames/ftir/mbtc8506.tof.

Appendix A: Correcting for stratospheric transport by use of N_2O

The OCS–N_2O relationship derived from MkIV balloon profiles (Fig. A1) is linear for $N_2O > 119$ ppb. A "knee" occurs at $N_2O = 119$ ppb, which corresponds to the $P_b = 10$ mbar pressure level at mid-latitudes (an altitude of ~ 30 km) and to $P_b = 20$ mbar (25 km altitude) in the high-latitude extra-vortex. Assume that

$$\mathrm{OCS}(p) = a[\mathrm{N_2O^{2K}}(p) - b] \quad \text{for } \mathrm{N_2O^{2K}} > b, \tag{A1a}$$

$$\mathrm{OCS}(p) = 0 \quad \text{for } \mathrm{N_2O^{2K}} < b. \tag{A1b}$$

p is the pressure, $b = 119$ ppb, $a = 0.00225$ is the gradient of the linear part of the OCS–N_2O^{2K} curve.

$$\mathrm{N_2O^{2K}}(p) = \mathrm{N_2O}(p, \text{year})/(1 + 0.0025(\text{year} - 2000)), \tag{A2}$$

where 0.0025 (0.25 %) is the annual rate of increase in N_2O.

The N_2O column is the integral of the N_2O mole fraction with respect to pressure

$$C^{2K}_{N_2O} = \int_0^{P_s} \mathrm{N_2O^{2K}}(p)/mg \, \mathrm{d}p \tag{A3}$$

where P_s is the surface pressure, m is the molar mass of air, and g is the acceleration due to gravity. The OCS column is the integral of the OCS mole fraction with respect to pressure

$$C_{OCS} = \int_0^{P_s} \mathrm{OCS}(p)/mg \, \mathrm{d}p. \tag{A4}$$

We split the pressure range at the knee in Fig. A1.

$$C_{OCS} = \int_0^{P_b} \mathrm{OCS}(p)/mg \, \mathrm{d}p + \int_{P_b}^{P_s} \mathrm{OCS}(p)/mg \, \mathrm{d}p \tag{A5}$$

where P_b is the pressure level above which OCS is zero, which means that the first term on the RHS of Eq. (A5) is zero by definition. Substituting for OCS(p) from Eq. (A1) yields

$$C_{OCS} = \int_{P_b}^{P_s} a[\mathrm{N_2O^{2K}}(p) - b]/mg \, \mathrm{d}p \tag{A6}$$

where the integration limits are now P_b to P_s since OCS is zero between 0 and P_b.

Assuming a linear relationship between N_2O and pressure between $p = 0$ and P_b, as seen in Fig. A2, then the N_2O column above P_b is $bP_b/2/(mg)$, which means that the OCS column is

$$C_{OCS} = a\left[C^{2K}_{N_2O} - b\,(P_s - P_b/2)\,/mg\right]. \tag{A7}$$

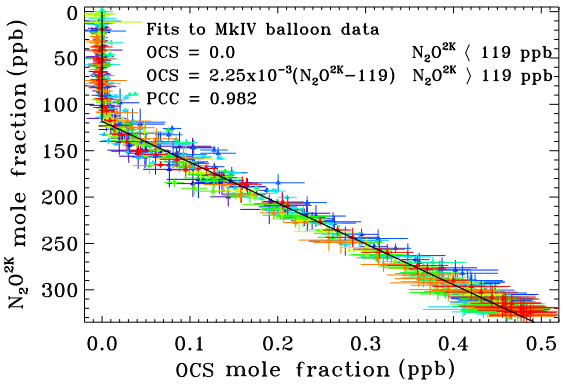

Figure A1. The MkIV balloon OCS–N_2O^{2K} relationship color-coded by year (blue: 1991; green: 2001; red: 2011) and the fitted straight-line segments (black). The line fitted to the $N_2O^{2K} > 119$ ppb data (417 points) has a gradient of 0.225 ± 0.001, an intercept of $N_2O = 119 \pm 4$ ppb, and a Pearson correlation coefficient of 0.982.

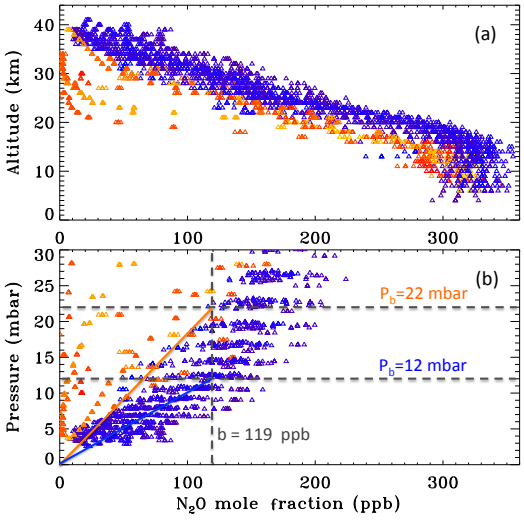

Figure A2. MkIV N_2O profiles, color-coded by latitude (blue: 35° N; red: 67° N). The top panel looks similar to the OCS profiles in Fig. 2b. The bottom panel shows the same N_2O data, but plotted versus pressure, and illustrates the linear relationship between N_2O and pressure at the highest altitudes. The horizontal banding is an artifact of the 1 km vertical grid used in the retrieval. The solid blue line represents the linear N_2O–pressure relationship assumed for the mid-latitude balloon flights. The orange line shows the N_2O–P relationship assumed for the extra-vortex high-latitude balloon flights.

Since P_b is only 10–20 mbar as compared with ~ 1000 mbar for P_s, this means that the second term, $b(P_s - P_b/2)/mg$, in Eq. (A7) is only about a third of the size of the first term (C_{N_2O}), and so the fractional change in C_{OCS} for a doubling of P_b from 10 to 20 mbar is only 0.75 %. So the P_b term tends to be unimportant. This is another

way of saying that the OCS–N_2O relationship is linear for 119 ppb $< N_2O <$ 320 ppb, which typically represents over 99 % of the N_2O column and over 99.9 % of the OCS column. So the nonlinearity above 30 km, or uncertainty in the "knee" altitude, does not have an important impact on C_{OCS}.

By substituting the measured N_2O column, de-trended to the year 2000, into Eq. (A7) we can predict the OCS column. This prediction encapsulates the stratospheric transport effects. By subtracting the predicted OCS, C^{P}_{OCS}, from the actual measured OCS column, C^{M}_{OCS},

$$\Delta_{OCS} = C^{M}_{OCS} - C^{P}_{OCS},$$
$$\Delta_{OCS} = C^{M}_{OCS} - a[C^{2K}_{N_2O} - b(P_s - P_b/2)/mg], \quad \text{(A8)}$$

we can derive an OCS anomaly, Δ_{OCS}, representing variations in OCS occurring below the altitudes covered by the balloon-derived OCS–N_2O relationship. By dividing Δ_{OCS} by C^{M}_{OCS}, we get a dimensionless quantity. Positive values indicate that the tropospheric OCS is in excess of the N_2O-based prediction.

Appendix B: Selection of ground-based OCS windows

Initially, 21 OCS windows were defined and evaluated in each ground-based spectrum, all located in the strong ν_3 band (See Table B1). None of the weaker OCS bands (at 868, 2915, and 4096 cm^{-1}) were used in the ground-based analyses because their OCS absorptions are simply too weak and/or overlapped with interfering absorptions. Of these 21 windows, 4 were new and 17 had been used previously. In the latter category are the two windows used by Griffith et al. (1998) for analysis of spectra from Wollongong and Lauder, three windows used by Rinsland et al. (2002) for analysis of ground-based Kitt Peak spectra (2.1 km altitude) and subsequently used by Mahieu et al. (2003) for analysis of Jungfraujoch (JFJ) spectra, four windows used by Krysztofiak et al. (2015) for analysis of ground-based OCS from Paris, four windows used by Kremser et al. (2015) for analysis of three Southern Hemisphere sites, and four windows used by Lejeune et al. (2017) for analysis of spectra from JFJ.

Table B1 summarizes the attributes of the 21 tested windows, including their center wavenumber, width, and fitted gases. Also included are the OCS line strengths (mean, max & sum) and their mean, strength-weighted, Ground State Energy (E''). Figure B1 plots the wavenumber extent of each window above a ground-based spectral fit to most of the OCS band.

In all the 17 previously used windows, there were several instances of close similarity: for example, the P_{25} line at $\sim$2051.32 cm^{-1} was used by everyone except Griffith et al. (1998). Surprisingly, the OCS R-branch has never previously been used for ground-based OCS retrievals, to the best of our knowledge, despite the lines being slightly stronger than those in the P-branch and more closely spaced.

Lejeune et al. (2017) gave a detailed description of their window selection and optimization process. Their initial selection was based on minimizing overlap with interfering absorptions, especially H_2O, under the conditions experienced at JFJ at 3.58 km altitude. Surprisingly, the OCS lines ranked first (2055.86 cm^{-1}) and fourth (2052.72 cm^{-1}) in Lejeune's listing of telluric non-interference were not utilized in their analysis of the full 20-year JFJ dataset. And the OCS line ranked 15th (2054.53 cm^{-1}) was used by Lejeune et al. (2017), despite being substantially overlapped by H_2O, which severely degrades this particular window at sites that are significantly warmer or lower in altitude than JFJ. Their final window selection was based on DOFs and information content.

In addition to these 17 previously used windows, in the present work four new, much-broader, windows were also evaluated. In these broad windows, most of the OCS lines are overlapped by stronger interfering absorbers, which would disqualify them in the traditional NDACC infrared working group window selection process. We argue here, however, that mere overlap with an interfering absorption is not sufficient grounds for exclusion. Provided the residual is reasonably small, an overlapped OCS line can still provide useful information.

Of the four new windows, the one centered at 2060 cm^{-1} covers the whole band. This includes some saturated H_2O lines at 2060.48 and 2065.50 cm^{-1} (see Fig. B1), which tend to give rise to large residuals affecting nearby OCS lines. When these saturated H_2O lines are excluded from the fits, by splitting the wide window into two, resulting in the broad windows centered at 2051 and 2070 cm^{-1}, the residuals improve considerably (from 0.55 to 0.40 %) with only a small loss of OCS information. This results in a better overall retrieval accuracy, and hence smaller uncertainties in the derived window-to-window biases.

All 21 candidate OCS windows were run through the full ground-based MkIV dataset, comprising 1090 observation days at 12 different sites. A statistical analysis was then performed on the column amounts retrieved by the GFIT algorithm. Each window was assumed to have a scale factor, Λ_j, such as might arise due to multiplicative errors in the spectral line strengths. And for each spectrum there is an average value of the retrieved geophysical quantity $\overline{Y}_i$, which might represent a vertical column abundance or the scale factor that multiplies the a priori VMR profile. Λ_j and $\overline{Y}_i$ are found by iteratively minimizing the quantity

$$\chi^2 = \sum_{j=1}^{N_W} \sum_{i=1}^{N_S} \left(\frac{Y_{i,j} - \Lambda_j \overline{Y}_i}{\varepsilon_{i,j}} \right)^2,$$

where i is an index over spectra and j is an index over windows. N_S is the number of spectra. N_W is the number of windows, 21 in the case of OCS. $Y_{i,j}$ is the measured value (e.g., column abundance) retrieved from the ith spectrum using the jth window of a particular gas, and $\varepsilon_{i,j}$ is its uncer-

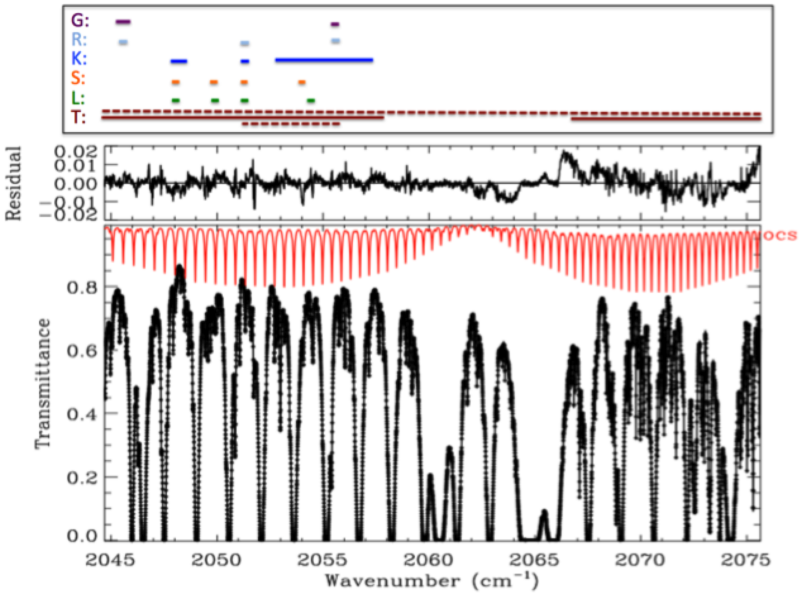

Figure B1. Spectral coverage of the evaluated windows superimposed above a fit to a ground-based MkIV spectrum measured from JPL at 58° SZA. The black points and line are the measured and calculated spectra, respectively. The red trace shows the OCS absorption, and the strong lines extend from P_{38} on the left to R_{36} on the right. In the top panel, the horizontal bars show the coverage of the windows evaluated in the study. G represents the windows used by Griffith et al. (1998), R by Rinsland et al. (2002), and so on. The brown solid lines labeled T were considered the best. The brown dotted lines were evaluated but rejected. This figure omits window no. 6 centered on the P_{50} line at 2038.95 cm^{-1}, used by Krysztofiak et al. (2015).

tainty (basically the square root of the diagonal element of $(\mathbf{K}^{\mathrm{T}}\mathbf{S}_y\mathbf{K})^{-1}$, where $\mathbf{K}$ is the Jacobian matrix and $\mathbf{S}_y$ is the measurement covariance matrix, estimated from the spectral fits). Hence the minimization obtains $N_{\mathrm{W}} + N_{\mathrm{S}}$ unknowns from $N_{\mathrm{W}} \cdot N_{\mathrm{S}}$ data points, so the solution is fully determined provided that $N_{\mathrm{W}} \geq 2$ and $N_{\mathrm{S}} \geq 2$. Since Λ_j and $\overline{Y}_i$ multiply each other, the problem is nonlinear, and so the solution must be found iteratively. If there are no biases between windows, Λ_j will be equal to the unit vector, and so the equation reduces to the usual definition of the mean: the value that minimizes the standard deviation of the points about it. If the uncertainties $\varepsilon_{i,j}$ are a true representation of the scatter of $Y_{i,j}$ about the mean, then the term in parentheses will have an average value of ~ 1, and so the χ^2 will have a value of $N_{\mathrm{W}} \cdot N_{\mathrm{S}} = N_{\mathrm{T}}$.

The results of this analysis are presented in Table B2. Firstly, the average RMS spectral residuals (Fit %) are reported for each window. These tend to be small for the narrow windows and larger for the wide windows. This is because the narrow windows were previously optimized to avoid large residuals. The average scale factor (Λ_j) of each window was computed with respect to the mean of all 21 windows. Departures from the ideal value of 1.0 can be considered a bias. The $\overline{\varepsilon}_j$ tells us the average uncertainty in the retrieved OCS column from the jth window.

We also computed the χ^2/N_{T}, the factor by which the scatter of the measurements compares with their uncertainties estimated from the spectral fits ($\overline{\varepsilon}_j$). In a perfect world χ^2/N_{T} would be close to 1.0. Values of χ^2/N_{T} that are significantly less than 1 imply a persistent systematic error in the spectral fits (e.g., line position error) that drives up $\overline{\varepsilon}_j$ but does not impair the precision of the measurements. Values of χ^2/N_{T} that are significantly > 1 imply more spectrum-to-spectrum scatter of the retrieved OCS than would be expected from the quality of the spectral fits. This could arise, for example, from an interfering T-dependent H_2O absorption blended with the OCS line. So $\overline{\varepsilon}_j \cdot \chi^2/N_{\mathrm{T}}$ provides an estimate of the precision of the measurements.

We also computed Pearson correlation coefficients (PCCs) between the 21 evaluated ground-based OCS windows and each other, and with the mean. In the interest of Table B2 being printable, we omit the 21 columns containing the window-to-window PCCs and show only the window-to-mean PCCs. Note that these are the correlations in the variations of xOCS. Total column OCS would produce much larger PCCs due to the fact that surface pressure changes (primarily driven by changes in observation altitude) would induce additional highly correlated changes between windows.

We now discuss how the information in Table B2 is used to select the best windows. Regarding the Λ_j values, window nos. 1, 3, and 6 are clearly biased low by more than their average uncertainties ($\overline{\varepsilon}_j$). And window no. 19 is biased high. These significant biases imply a problem with the spectroscopy, and so it would be a risk to use these windows until the cause of the bias is identified. So these four windows are rejected. In terms of their $\overline{\varepsilon}_j$ values, window nos. 6

Table B1. Attributes of the 21 ground-based OCS spectral windows evaluated on MkIV ground-based spectra. Center and Width are in units of cm^{-1}. Windows 1–17 represent old, previously used windows and are grouped chronologically by reported use. Windows 1–2 were defined by Griffith et al. (1998); 3–5 by Rinsland et al. (2002); 6–9 by Krysztofiak et al. (2015); 10–13 by Kremser et al. (2015); and 14–17 by Lejeune et al. (2017). Windows 18–21 are the new ones. The fitted OCS lines are all from the ν_3 band. The column labeled Lines shows the spectroscopic assignment of the strongest OCS lines in each window (exceeding 1 % absorption depth). The number of such lines is simply the difference of the quantum numbers plus 1. So window no. 20 contains $38+36+1=75$ lines. Window no. 21 contains $36-11+1=26$ lines. S_{max} is the maximum OCS line intensity in units of cm^{-1} (molec cm^{-2})$^{-1}$, $\sum S$ is the sum of intensities, and S_{bar} is the mean (S-weighted) intensity. E'' is the mean (S-weighted) ground state energy. co2(2) refers to $^{13}CO_2$; h2o(2) refers to HDO. The attributes tabulated below are all independent of the measured spectra.

No. (j)	Center (cm^{-1})	Width (cm^{-1})	Lines	Fitted interfering gases	S_{max} $\times 10^{-18}$	$\sum S$ $\times 10^{-18}$	S_{bar} $\times 10^{-18}$	E'' (cm^{-1})
1^G	2045.485	0.65	P_{37}	ocs o3 co2 co	0.816	1.134	0.606	366
2^G	2055.805	0.33	P_{15}	ocs o3 co2 co	1.050	1.137	0.972	74
3^R	2045.485	0.37	P_{37}	ocs o3 co2 co	0.816	1.046	0.654	368
4^R	2051.330	0.30	P_{25}	ocs o3 h2o co2	1.165	1.226	1.109	137
5^R	2055.800	0.32	P_{15}	ocs o3 co2 co	1.050	1.137	0.972	74
6^K	2038.950	0.30	P_{50}	ocs o3 h2o co2	0.356	0.392	0.324	558
7^K	2048.250	0.90	P_{32}–P_{31}	ocs o3 h2o co2 co	1.030	2.530	0.826	270
8^K	2051.400	0.40	P_{25}	ocs o3 h2o co2 co	1.176	1.367	1.001	181
9^K	2054.950	4.90	P_{22}–P_{12}	ocs o3 h2o co2 co	1.183	13.61	0.966	117
10^S	2048.000	0.44	P_{32}	ocs o3 co2	0.998	1.251	0.815	278
11^S	2049.935	0.37	P_{28}	ocs o3 co2(2) co	1.112	1.323	0.926	224
12^S	2051.330	0.29	P_{25}	ocs o3 h2o co2	1.165	1.226	1.109	137
13^S	2054.110	0.26	P_{19}	ocs o3 co2 h2o co	1.157	1.222	1.096	109
14^L	2048.045	0.39	P_{32}	ocs o3 co2	0.998	1.244	0.815	278
15^L	2049.975	0.41	P_{28}	ocs o3 co2(2) co	1.112	1.350	0.926	224
16^L	2051.320	0.28	P_{25}	ocs o3 h2o co2	1.165	1.226	1.109	137
17^L	2054.500	0.34	P_{18}	ocs o3 co2 h2o(2)	1.139	1.234	1.054	101
18^T	2051.300	13.10	P_{38}–P_{11}	ocs o3 h2o co2 co	1.183	35.23	0.882	203
19^T	2053.550	4.80	P_{25}–P_{15}	ocs o3 h2o co2 co	1.183	14.26	1.018	134
20^T	2060.170	30.95	P_{38}–R_{36}	ocs o3 h2o co2 co	1.248	85.02	0.833	208
21^T	2071.100	9.00	R_{11}–R_{36}	ocs o3 h2o co2 co	1.248	33.96	0.978	204

and 17 both exceed 5 %, and although there is nothing inherently malign in such high values, these windows will eventually be outweighed by the others with much smaller uncertainties during the subsequent averaging over windows. So since these windows will negligibly impact the final OCS results, they are better omitted. The χ^2/N_T values exceed 1 for window nos. 7 and 17, implying more spectrum-to-spectrum scatter of the retrieved OCS than would be expected based on the quality of the spectral fits, which is a cause for concern.

We should point out that all the parameters in Table B2 except $\overline{\varepsilon}_j$ depend on comparing a particular window with the mean of all windows. So when the list of windows includes some very similar variants on the same window (e.g., 2051 cm^{-1}), this has a disproportionate weight on the average, tends to increase the PCC, and brings the Λ_j closer to 1.0. And since 19 of the windows occupy the P-branch and only 1 solely utilizes the R-branch, we should expect this window to have a poorer bias and a lower PCC. So it is surprising to see window no. 21 do so well, with a bias of < 1 % and a PCC of 0.83. And its χ^2/N_T value of 0.33 is the lowest of all windows, implying that although systematic errors increased the residuals and hence $\overline{\varepsilon}_j$, this did not affect the precision, which at 0.007 % is the best of all windows.

Of the four Lejeune windows, window no. 17 containing the P_{18} line at 2054.50 cm^{-1} stands out as clearly the worst, at least for the purpose of analyzing MkIV spectra. This is based on multiple factors, including a 1.9 % bias in its Λ_j, its large (5 %) uncertainty, its χ^2/N_T exceeding 1, and a PCC of only 0.64, which is the lowest in the entire table. This poor performance is likely related to the contamination of this window by H_2O in the lower-altitude MkIV spectra. This window was rated fifteenth best in Table 1 of Lejeune et al. (2017), an assessment with which we concur, but was nevertheless one of four that they eventually selected for use.

Window no. 6 containing the P_{50} line at 2038.95 cm^{-1} is another poor performer. There is a 9.1 % low bias in the

Table B2. Statistical properties of the OCS retrievals from the 21 investigated windows. Center and Width are as in Table B1. Fit is the average RMS spectral fitting residual achieved in that particular window. Of course, this depends on the spectra that are fitted (their altitude, SZA, spectral resolution, etc.), and so its absolute value is somewhat arbitrary, but its window-to-window variation is significant since all windows were fitted in all spectra. Λ_j is the average value of the OCS VMR scale factor retrieved from window j, relative to the mean of all windows. $\overline{\varepsilon}_j$ is an estimate of the mean uncertainty associated with retrieving OCS from window j, based on the spectral fits. X^2/N_T represents the average value of the ratio of the scatter of the measurements from the mean to the estimated uncertainty. $\overline{\varepsilon}_j \cdot \chi^2/N_T$ represents the precision of the measurements. The column labeled PCC contains Pearson correlation coefficients of xOCS variations between each evaluated ground-based window and the mean of all windows. Based on these diagnostics, OCS columns retrieved from window nos. **18** and **21** were selected and averaged for subsequent analysis, with the other 19 windows discarded.

No. (j)	Center (cm^{-1})	Width (cm^{-1})	Fit (%)	Λ_j	$\overline{\varepsilon}_j$	χ^2/N_T	$\overline{\varepsilon}_j \cdot \chi^2/N_T$	PCC
1^G	2045	0.65	0.190	0.964	0.030	0.73	0.022	0.790
2^G	2055	0.33	0.215	1.013	0.029	0.57	0.017	0.827
3^R	2045	0.37	0.171	0.952	0.036	0.66	0.024	0.811
4^R	2051	0.30	0.148	0.997	0.014	0.76	0.011	0.798
5^R	2055	0.32	0.215	1.015	0.030	0.57	0.017	0.827
6^K	2038	0.30	0.125	0.909	0.053	0.75	0.040	0.702
7^K	2048	0.90	0.229	0.991	0.015	1.15	0.017	0.786
8^K	2051	0.40	0.181	0.995	0.017	0.92	0.016	0.774
9^K	2054	4.90	0.373	1.014	0.017	0.70	0.011	0.829
10^S	2048	0.44	0.196	0.984	0.020	0.67	0.013	0.835
11^S	2049	0.37	0.195	1.011	0.025	0.63	0.016	0.827
12^S	2051	0.29	0.144	0.997	0.014	0.74	0.011	0.794
13^S	2054	0.26	0.150	0.986	0.030	0.77	0.023	0.791
14^L	2048	0.39	0.182	1.002	0.023	0.78	0.018	0.825
15^L	2049	0.41	0.190	1.012	0.025	0.62	0.015	0.835
16^L	2051	0.28	0.145	0.998	0.014	0.65	0.010	0.803
17^L	2054	0.34	0.195	0.981	0.051	1.09	0.056	0.640
18^T	**2051**	**13.1**	**0.394**	**1.009**	**0.015**	**0.54**	**0.008**	**0.840**
19^T	2053	4.80	0.395	1.024	0.018	0.65	0.012	0.846
20^T	2060	30.9	0.552	0.987	0.021	0.49	0.010	0.855
21^T	**2071**	**9.0**	**0.417**	**1.005**	**0.021**	**0.33**	**0.007**	**0.831**

retrieved OCS amounts, the worst of all windows, and the uncertainties are over 5 %, on average, despite having the smallest RMS residual. Its PCC of 0.70 is the second lowest. We suggest that the poor performance of this window relates to the weakness of the P_{50} OCS line and its large E'' value (558 cm^{-1}).

The P_{15} line at 2055.8 cm^{-1} was used by Griffith et al. (1998; window no. 2) and Rinsland et al. (2002; window no. 5), but not by Kremser et al. (2015) or Lejeune et al. (2017), despite this window being rated first of the 21 in Table 1 of Lejeune et al. (2017). In our work we find this to be one of the better narrow windows, but not the best.

The best narrow windows were those centered on the P_{25} line at 2051.4 cm^{-1}. Considering that it contains only one OCS line, the various narrow 2051 cm^{-1} windows do remarkably well. Its spectral fits are more than a factor 2 better than the wide 2051.30 cm^{-1} window containing 28 lines. Consequently the computed $\overline{\varepsilon}_j$ of the narrow and wide 2051 cm^{-1} windows is the same. The wide window has lower χ^2/N_T and consequently higher precision, and superior correlation coefficients.

Based on Table B2, we opted to use the two broad windows centered at 2051 and 2071 cm^{-1} (no. 18 and no. 21, bold) for the final OCS retrievals whose results are used in the paper. Of the four wide windows in the lower half of the table, these two give the Λ_j values closest to 1.0 and have the best precisions ($\overline{\varepsilon}_j \cdot \chi^2/N_T$).

Appendix C: Selection of ground-based N_2O windows

A study was performed on 15 candidate N_2O windows covering 2400 to 4800 cm^{-1}. These windows include (1) three traditional, narrow, MIR windows used by NDACC, (2) nine recently defined broader MIR windows, and (3) three broad shortwave infra-red windows used by TCCON. Table C1 de-

Table C1. Attributes of the 15 ground-based N_2O spectral windows that were tested using MkIV ground-based spectra. Band defines the N_2O band with the dominant lines in this window. Lines denotes the transition quantum numbers. S_{max} is the maximum N_2O line, $\sum S$ is the sum of intensities, and S_{bar} is the mean (S-weighted) intensity, all in units of 10^{-21} cm^{-1} (molec cm^{-2})$^{-1}$. E'' is the mean (S-weighted) ground state energy in units of cm^{-1}. These attributes are all independent of the measured spectra. A [a] in column 1 denotes windows that were accepted for subsequent analysis. A [b] in column 1 denotes windows whose averaging kernels are plotted in Fig. C1.

No.	Center (cm^{-1})	Width (cm^{-1})	N_2O band	Lines	Fitted interfering gases	S_{max}	$\sum S_i$	S_{bar}	E'' (cm^{-1})
1[a]	2443.10	2.60	$\nu_3+2\nu_2$	P_{23}–P_{21}	co2	4.56	15.9	3.67	312
2[a]	2481.85	1.30	$\nu_3+2\nu_2$	R_{23}		4.40	9.7	3.83	322
3	2806.32	0.44	$\nu_1+\nu_2$	R_9	ch4	0.77	0.8	0.77	38
4[a]	2446.00	26.20	$\nu_3+2\nu_2$	P_{33}–P_4	co2 ch4 hdo h2o	5.08	135.0	3.52	257
5[a, b]	2479.70	19.80	$\nu_3+2\nu_2$	R_9–R_{33}	co2 ch4 hdo h2o	5.48	123.0	3.99	278
6[b]	2539.80	46.60	$2\nu_3$	P_{47}–P_1	hdo h2o ch4 co2	22.5	619.0	15.4	252
7	2580.40	34.60	$2\nu_3$	R_0–R_{51}	hdo h2o ch4 co2	24.3	713.0	15.9	261
8[a, b]	2781.70	25.20	$\nu_1+\nu_2$	P_{31}–P_5	hdo h2o ch4 co2 o3 hcl	0.71	0.3	0.35	436
9	2796.95	5.30	$\nu_1+\nu_2$	Q_{39}–R_0	hdo h2o ch4 co2 o3 hcl	1.59	41.0	1.16	191
10[a]	2813.00	26.80	$\nu_1+\nu_2$	R_1–R_{38}	hdo h2o ch4 co2 o3 hcl	0.88	24.2	0.62	230
11[a]	3344.40	2.48	$\nu_1+2\nu_2$	P_{23}–P_{21}	1h2o h2o co2 hcn	1.36	4.2	1.22	251
12[a]	3372.70	2.20	$\nu_1+2\nu_2$	R_9–R_{11}	1h2o h2o co2 hdo	1.53	4.6	1.40	101
13[a, b]	4395.20	43.40	$2\nu_1$	P_{39}–P_1	ch4 h2o hdo	1.13	33.2	0.72	278
14[a]	4430.10	23.10	$2\nu_1$	R_1–R_{49}	ch4 h2o hdo co2	1.17	30.1	0.86	196
15[a]	4719.45	73.00	$2\nu_1+\nu_2$	P_{42}–R_{56}	ch4 h2o co2	0.73	40.0	0.47	261

Table C2. Statistical properties of the N_2O retrievals and xN_2O amounts retrieved from the 15 investigated windows. The symbols Λ_j, $\overline{\varepsilon}_j$, and χ^2/N are defined in Appendix B. Windows in bold font denote those accepted in the subsequent analyses. So 11 windows were accepted and 4 were not. The PCC values are generally smaller than those of OCS, reflecting the smaller variations in atmospheric xN_2O in comparison with the measurement noise.

No.	Center (cm^{-1})	Width (cm^{-1})	Fit %	Λ_j	$\overline{\varepsilon}_j$	χ^2/N_T	$\overline{\varepsilon}_j \cdot \chi^2/N_T$	PCC
1	**2443.1**	**2.6**	**0.136**	**0.9914**	**0.0052**	**0.399**	**0.0021**	**0.758**
2	**2481.8**	**1.3**	**0.148**	**0.9938**	**0.0053**	**0.463**	**0.0025**	**0.760**
3	2806.3	0.4	0.138	0.9907	0.0133	0.906	0.0120	0.591
4	**2446.0**	**26.2**	**0.205**	**0.9925**	**0.0066**	**0.319**	**0.0019**	**0.802**
5	**2479.7**	**19.8**	**0.187**	**0.9949**	**0.0055**	**0.361**	**0.0020**	**0.800**
6	2539.8	46.6	0.277	1.0053	0.0080	0.838	0.0067	0.770
7	2580.4	34.6	0.349	1.0070	0.0101	0.612	0.0062	0.785
8	**2781.7**	**25.2**	**0.414**	**1.0038**	**0.0164**	**0.644**	**0.0100**	**0.758**
9	2796.9	5.3	0.416	1.0553	0.0142	0.888	0.0130	0.743
10	**2814.0**	**29.8**	**0.434**	**1.0068**	**0.0167**	**0.498**	**0.0084**	**0.789**
11	**3344.4**	**2.5**	**0.208**	**1.0241**	**0.0112**	**0.662**	**0.0073**	**0.604**
12	**3372.7**	**2.2**	**0.190**	**1.0329**	**0.0089**	**0.833**	**0.0074**	**0.620**
13	**4395.2**	**43.4**	**0.374**	**0.9874**	**0.0141**	**0.490**	**0.0069**	**0.767**
14	**4430.1**	**23.1**	**0.328**	**0.9895**	**0.0121**	**0.537**	**0.0063**	**0.755**
15	**4719.4**	**73.1**	**0.297**	**0.9990**	**0.0114**	**1.010**	**0.0115**	**0.662**

fines these 15 windows and the fitted parameters, together with their key attributes.

No windows from the super-strong N_2O ν_1 band centered at 2224 cm^{-1} were evaluated. These are saturated in ground-based spectra, even at low air masses. The windows at 2539 and 2580 cm^{-1} contain the strongest lines, a factor 4 stronger than the four next strongest windows in the 2400–2500 cm^{-1} region. The 2781 cm^{-1} window contains the weakest lines, closely followed by the 4719 cm^{-1} TCCON window. Our philosophy is to have windows with a range of different line strengths to cover low- and high-air-mass conditions. But there is another consideration: we want N_2O averaging kernels to match those of OCS, which requires favoring the win-

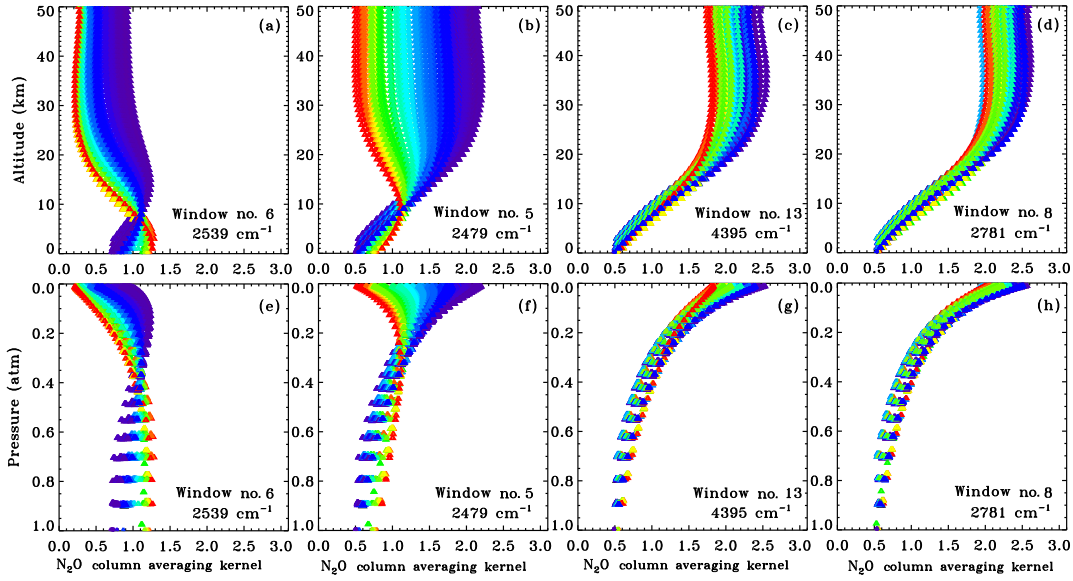

Figure C1. Averaging kernels for four N_2O windows color-coded by air mass. Red denotes an air mass of 9, orange 7, green 5, cyan 3, blue 2, and purple 1. Panels **(a, b, c, d)** plot kernels versus altitude; **(e, f, g, h)** plot the same kernels versus pressure. Panels **(a, e)** show results for 2539 cm^{-1}, which we did not use in the final analysis because N_2O lines were too strong. Panels **(b, f)** show the less strong 2479 cm^{-1} window. Panels **(c, g)** show the medium strength 4395 cm^{-1} window. Panels **(d, h)** show kernels from the 2781 cm^{-1} window containing weak N_2O lines.

dows with the weaker N_2O lines that match the depths of the OCS lines.

These 15 windows were run through the MkIV ground-based dataset (4000+ spectra and 1000+ observation days), covering 12 different sites from 0 to 3.8 km altitude over 1985–2016. Table C2 summarizes the results for each window. Note that all windows were measured simultaneously in the same InSb spectrum.

The 2796 window (no. 9) has the most deviant Λ_j value (1.055). This window covers the Q-branch of the $\nu_1 + \nu_2$ band. The adjacent windows cover the P- and R-branches of the same band, but are bias-free. So perhaps the Q-branch is affected by line-mixing. Certainly the individual Q-branch lines are well overlapped in ground-based observations. Balloon observations (lower pressure, less line-mixing) reveal only a 1 % bias.

Table C2 also shows correlation coefficients between the retrieved xN_2O from each of the 15 N_2O windows, and the mean. A high PCC does not necessarily mean that a window is good. It just means that it consistently shows similar behavior to the mean of all windows. The broad 2446 and 2479 cm^{-1} windows (nos. 4 and 5) have the highest PCCs with mean values ≥ 0.8. The 2806 cm^{-1} window (no. 3) has the lowest PCC with a mean value of 0.59, which is probably related to its low E'' (= 38 cm^{-1}). Temperature-independent transitions have an E'' of $\sim$300 cm^{-1}, so an E'' of 38 cm^{-1} will allow errors in the assumed atmospheric temperature to induce additional variations in the retrievals not present in the other less T-sensitive windows. This will drive down the PCC, and also increase the χ^2/N_T.

The narrow windows containing a single N_2O line do very well in terms of their $\overline{\varepsilon}_j$. This is because you can achieve very good fits to a narrow window by avoiding large residuals due to poor spectroscopy of interferers or other factors (e.g., temperature, interfering H_2O). A broader window may have nine usable (i.e., non-saturated) N_2O lines, but if the fits are 3 × worse due to interferences, the computed retrieval uncertainty will be the same as the narrow window.

Figure C1 shows averaging kernels for four N_2O windows, with decreasing line intensities from left to right. In the upper panels the kernels are plotted as a function of altitude. In the lower panels the same kernels are plotted as a function of pressure. The kernels are computed for a representative subset of 140 ground-based spectra covering altitudes from 0 to 3.8 km, and temperatures from −40 to +40 °C. Kernels are color-coded by air mass (red high; blue low), the most important factor governing the shape.

In summary, we rejected the 2806 window (no. 3) based on its poor PCC, a likely consequence of its low E''. We rejected the 2796 cm^{-1} window (no. 9) because it currently produces a high bias of 6 % relative to the other windows, likely due to our neglect of line-mixing. We rejected the 2539 and 2580 cm^{-1} windows (nos. 6 and 7) because they are much stronger than the others and therefore have much smaller averaging kernels in the stratosphere. The remaining 11 N_2O windows were averaged, after correcting for their biases, and used to create the results presented in the paper.

The Supplement related to this article is available online at https://doi.org/10.5194/acp-18-1923-2018-supplement.

Competing interests. The authors declare that they have no conflict of interest.

Special issue statement. This article is part of the special issue "Twenty-five years of operations of the Network for the Detection of Atmospheric Composition Change (NDACC) (AMT/ACP/ESSD inter-journal SI)". It is not associated with a conference.

Acknowledgements. This research was performed at the Jet Propulsion Laboratory, California Institute of Technology, under contract with the National Aeronautics and Space Administration. We thank the Columbia Scientific Balloon Facility (CSBF) who conducted the majority of the balloon flights. We also thank the CNES Balloon Launch facility who conducted two MkIV balloon flights from Esrange, Sweden. We thank the Swedish Space Corporation for their support and our use of their facilities. Finally, we acknowledge support from the NASA Upper Atmosphere Research Program. Government sponsorship acknowledged.

Edited by: Hal Maring
Reviewed by: two anonymous referees

References

Barkley, M. P., Palmer, P. I., Boone, C. D., Bernath, P. F., and Suntharalingam, P.: Global distributions of carbonyl sulfide in the upper troposphere and stratosphere, Geophys. Res. Lett., 35, L14810, https://doi.org/10.1029/2008GL034270, 2008.

Berry, J., Wolf, A., Campbell, J. E., Baker, I., Blake, N., Blake, D., Denning, A. S., Kawa, S. R., Montzka, S. A., and Seibt, U.: A coupled model of the global cycles of carbonyl sulfide and CO_2: A possible new window on the carbon cycle, J. Geophys. Res.-Biogeo., 118, 842–852, 2013.

Brühl, C., Lelieveld, J., Tost, H., Höpfner, M., and Glatthor, N.: Stratospheric sulfur and its implications for radiative forcing simulated by the chemistry climate model EMAC, J. Geophys. Res.-Atmos., 120, 2103–2118, 2015.

Campbell, J. E., Carmichael, G. R., Chai, T., Mena-Carrasco, M., Tang, Y., Blake, D. R., Blake, N. J., Vay, S. A., Collatz, G. J., Baker, I., Berry, J. A., Montzka, S. A., Sweeney, C., Schnoor, J. L., and Stanier, C. O.: Photosynthetic control of atmospheric carbonyl sulfide during the growing season, Science, 322, 1085–1088, 2008.

Campbell, J. E., Whelan, M. E., Seibt, U., Smith, S. J., Berry, J. A., and Hilton, T. W.: Atmospheric carbonyl sulfide sources from anthropogenic activity: Implications for carbon cycle constraints, Geophys. Res. Lett., 42, 3004–3010, https://doi.org/10.1002/2015GL063445, 2015.

Crutzen, P. J.: The possible importance of COS for the sulfate layer of the stratosphere, Geophys. Res. Lett., 3 73–76, 1976.

Dlugokencky, E. J., Walter, B. P., Masarie, K. A., Lang, P. M., and Kasischke, E. S.: Measurements of an anomalous global methane increase during 1998, Geophys. Res. Lett., 28, 499-502, 2001.

Glatthor, N., Höpfner, M., Baker, I. T., Berry, J., Campbell, J. E., Kawa, S. R., Krysztofiak, G., Leyser, A., Sinnhuber, B.-M., Stiller, G. P., Stinecipher, J., and von Clarmann, T.: Tropical sources and sinks of carbonyl sulfide observed from space, Geophys. Res. Lett., 42, 10082–10090, 2015.

Glatthor, N., Höpfner, M., Leyser, A., Stiller, G. P., von Clarmann, T., Grabowski, U., Kellmann, S., Linden, A., Sinnhuber, B.-M., Krysztofiak, G., and Walker, K. A.: Global carbonyl sulfide (OCS) measured by MIPAS/Envisat during 2002–2012, Atmos. Chem. Phys., 17, 2631–2652, https://doi.org/10.5194/acp-17-2631-2017, 2017.

Griffith, D. W. T., Jones, N. B., and Matthews, W. A.: Interhemispheric ratio and annual cycle of carbonyl sulfide (OCS) total column from ground-based solar FTIR spectra, J. Geophys. Res., 103, 8447–8454, https://doi.org/10.1029/97JD03462, 1998.

Irion, F. W., Gunson, M. R., Toon, G. C., Chang, A. Y., Eldering, A., Mahieu, E., Manney, G. L., Michelsen, H. A., Moyer, E. J., Newchurch, M. J., Osterman, G. B., Rinsland, C. P., Salawitch, R. J., Sen, B., Yung, Y. L., and Zander, R.: Atmospheric Trace Molecule Spectroscopy (ATMOS) Experiment Version 3 data retrievals, Appl. Optics, 41, 6968–6979, 2002.

Kettle, A. J., Kuhn, U., von Hobe, M., Kesselmeier, J., and Andreae, M. O.: Global budget of atmospheric carbonyl sulfide: Temporal and spatial variations of the dominant sources and sinks, J. Geophys. Res., 107, 4658, https://doi.org/10.1029/2002JD002187, 2002.

Kremser, S., Jones, N. B., Palm, M., Lejeune, B., Wang, Y., Smale, D., and Deutscher, N. M.: Positive trends in Southern Hemisphere carbonyl sulfide, Geophys. Res. Lett., 42, 9473–9480, https://doi.org/10.1002/2015GL065879, 2015.

Krysztofiak, G., Veng Te, Y., Catoire, V., Berthet, G., Toon, G. C., Jégou, F., Jeseck, P., and Robert, C.: Carbonyl sulfide (OCS) variability with latitude in the atmosphere, Atmosphere-Ocean, 53, 89–101, https://doi.org/10.1080/07055900.2013.876609, 2015.

Kuai, L., Worden, J., Kulawik, S. S., Montzka, S. A., and Liu, J.: Characterization of Aura TES carbonyl sulfide retrievals over ocean, Atmos. Meas. Tech., 7, 163–172, https://doi.org/10.5194/amt-7-163-2014, 2014.

Kuai, L., Worden, J. R., Campbell, J. E., Kulawik, S. S., Li, K. F., Lee, M., Weidner, R. J., Montzka, S. A., Moore, F. L., and Berry, J. A.: Estimate of carbonyl sulfide tropical oceanic surface fluxes using Aura Tropospheric Emission Spectrometer observations, J. Geophys. Res.-Atmos., 120, 11012–11023, https://doi.org/10.1002/2015JD023493, 2015.

Lejeune, B., Mahieu, E., Vollmer, M. K., Reimann, S., Bernath, P. F., Boone, C. D., Walker, K. A., and Servais, C.: Optimized approach to retrieve information on atmospheric carbonyl sulfide (OCS) above the Jungfraujoch station and change in its abundance since 1995, J. Quant. Spectrosc. Ra., 186, 81–95, 2017.

Leung, F.-Y., Colussi, A. J., Hoffmann, M. R., and Toon, G. C.: Isotopic fractionation of Carbonyl sulphide in the atmosphere: Implications for the source of background stratospheric sulphate aerosol, Geophys. Res. Lett., 29, 1474, https://doi.org/10.1029/2001GL013955, 2002.

Mahieu, E., Rinsland, C. P., Zander, R., Duchatelet, P., Servais, C., and De Mazière, M.: Tropospheric and stratospheric carbonyl

sulfide (OCS): Long-term trends and seasonal cycles above the Jungfraujoch station, in: Proceedings of the "Sixth European Symposium on Stratospheric Ozone", Göteborg, Sweden, 2–6 September 2002, EUR 20650, 309–312, 2003.

Montzka, S. A., Hall, B., Elkins, J. W., Miller, L., Watson, A., Sweeney, C., and Tans, P. P.: On the global distribution, seasonality, and budget of atmospheric carbonyl sulfide (COS) and some similarities to CO_2, J. Geophys. Res., 112, D09302, https://doi.org/10.1029/2006JD007665, 2007.

Notholt, J., Toon, G. C., Lehmann, R., Sen, B., and Blavier, J.-F.: Comparison of Arctic and Antarctic trace gas column abundances from ground-based Fourier transform infrared spectrometry, J. Geophys. Res., 102, 12863–12869, https://doi.org/10.1029/97JD00358, 1997.

Notholt, J., Kuang, Z., Rinsland, C. P., Toon, G. C., Rex, M., Jones, N., Albrecht, T., Deckelmann, H., Krieg, J., Weinzierl, C., Bingemer, H., Weller, R., and Schrems, O.: Enhanced upper tropical tropospheric COS: Impact on the stratospheric aerosol layer, Science, 300, 307–310, 2003.

Rinsland, C. P., Goldman, A., Mahieu, E., Zander, R., Notholt, J., Jones, N. B., Griffith, D. W. T., Stephen, T. M., and Chiou, L. S.: Ground-based infrared spectroscopic measurements of carbonyl sulfide: Free tropospheric trends from a 24-year time series of solar absorption measurements, J. Geophys. Res., 107, 4657, https://doi.org/10.1029/2002JD002522, 2002.

Rinsland, C. P., Dufour, G., Boone, C. D., Bernath, P. F., Chiou, L., Coheur, P.-F., Turquety, S., and Clerbaux, C.: Satellite boreal measurements over Alaska and Canada during June–July 2004: Simultaneous measurements of upper tropospheric CO, C_2H_6, HCN, CH_3Cl, CH_4, C_2H_2, CH_3OH, HCOOH, OCS, and SF_6 mixing ratios, Global Biogeochem. Cy., 21, GB3008, https://doi.org/10.1029/2006GB002795, 2007.

Rinsland, C. P., Chiou, L., Mahieu, E., Zander, R., Boone, C. D., and Bernath, P. F.: Measurements of long-term changes in atmospheric OCS (carbonyl sulfide) from infrared solar observations, J. Quant. Spectrosc. Ra., 109, 2679–2686, 2008.

Rothman L. S., Gordon, I. E., Babikov, Y., Barbe, A., Benner, D. C., Bernath, P. F., Birk, M., Bizzocchi, L., Boudon, V., Brown, L. R., Campargue, A., Chance, K., Cohen, E. A., Coudert, L. H., Devi, V. M., Drouin, B. J., Fayt, A., Flaud, J.-M., Gamache, R. R., Harrison, J. J., Hartmann, J.-M., Hill, C., Hodges, J. T., Jacquemart, D., Jolly, A., Lamouroux, J., LeRoy, R. J., Li, G., Long, D. A., Lyulin, O. M., Mackie, C. J., Massie, S. T., Mikhailenko, S., Müller, H. S. P., Naumenko, O. V., Nikitin, A. V., Orphal, J., Perevalov, V., Perrin, A., Polovtseva, E. R., Richard, C., Smith, M. A. H., Starikova, E., Sung, K., Tashkun, S., Tennyson, J., Toon, G. C., Tyuterev, Vl. G., and Wagner, G.: The HITRAN2012 Molecular Spectroscopic Database, J. Quant. Spectrosc. Ra., 130, 4–50, 2013.

Sen, B., Toon, G. C., Blavier, J.-F., Fleming, E. L., and Jackman, C. H.: Balloon-borne observations of mid-latitude fluorine abundance, J. Geophys. Res., 101, 9045–9054, 1996.

Toon, G. C.: The JPL MkIV Interferometer, Opt. Photonics News, 2, 19–21, 1991.

Toon, G. C.: Telluric line list for GGG2014, TCCON data archive, hosted by the Carbon Dioxide Information Analysis Center, Oak Ridge National Laboratory, USA, https://doi.org/10.14291/tccon.ggg2014.atm.R0/1221656, 2014a.

Toon, G. C.: Solar line list for GGG2014, TCCON data archive, hosted by the Carbon Dioxide Information Analysis Center, Oak Ridge National Laboratory, USA, https://doi.org/10.14291/tccon.ggg2014.atm.R0/1221658, 2014b.

Toon, G. C., Blavier, J.-F., Sen, B., Margitan, J. J., Webster, C. R., May, R. D., Fahey, D. W., Gao, R., Del Negro, L., Proffitt, M., Elkins, J., Romashkin, P. A., Hurst, D. F., Oltmans, S., Atlas, E., Schauffler, S., Flocke, F., Bui, T. P., Stimpfle, R. M., Bonne, G. P., Voss, P. B., and Cohen, R. C.: Comparison of MkIV balloon and ER-2 aircraft profiles of atmospheric trace gases, J. Geophys. Res., 104, 26779–26790, 1999.

Toon, G. C., Blavier, J.-F., Sung, K., Rothman, L. S., and Gordon, I.:, HITRAN spectroscopy evaluation using solar occultation FTIR spectra, J. Quant. Spectrosc. Ra., 182, 324–336, https://doi.org/10.1016/j.jqsrt.2016.05.021, 2016.

Velazco, V. A., Toon, G. C., Blavier, J.-F. L., Kleinbohl, A., Manney, G. L., Daffer, W. H., Bernath, P. F., Walker, K. A., and Boone, C.: Validation of the Atmospheric Chemistry Experiment by noncoincident MkIV balloon profiles, J. Geophys. Res., 116, D06306, https://doi.org/10.1029/2010JD014928, 2011.

Vincent, R. A. and Dudhia, A.: Fast retrievals of tropospheric carbonyl sulfide with IASI, Atmos. Chem. Phys., 17, 2981–3000, https://doi.org/10.5194/acp-17-2981-2017, 2017.

Wang, Y., Deutscher, N. M., Palm, M., Warneke, T., Notholt, J., Baker, I., Berry, J., Suntharalingam, P., Jones, N., Mahieu, E., Lejeune, B., Hannigan, J., Conway, S., Mendonca, J., Strong, K., Campbell, J. E., Wolf, A., and Kremser, S.: Towards understanding the variability in biospheric CO_2 fluxes: using FTIR spectrometry and a chemical transport model to investigate the sources and sinks of carbonyl sulfide and its link to CO_2, Atmos. Chem. Phys., 16, 2123–2138, https://doi.org/10.5194/acp-16-2123-2016, 2016.

Wang, Z., Deutscher, N. M., Warneke, T., Notholt, J., Dils, B., Griffith, D. W. T., Schmidt, M., Ramonet, M., and Gerbig, C.: Retrieval of tropospheric column-averaged CH_4 mole fraction by solar absorption FTIR-spectrometry using N_2O as a proxy, Atmos. Meas. Tech., 7, 3295–3305, https://doi.org/10.5194/amt-7-3295-2014, 2014.

Wilson, J. C., Lee, S.-H., Reeves, J. M., Brock, C. A., Jonsson, H. H., Lafleur, B. G., Loewenstein, M., Podolske, J., Atlas, E., Boering, K., Toon, G., Fahey, D., Bui, T. P., Diskin, G., and Moore, F.: Steady-state aerosol distributions in the extra-tropical, lower stratosphere and the processes that maintain them, Atmos. Chem. Phys., 8, 6617–6626, https://doi.org/10.5194/acp-8-6617-2008, 2008.

Wunch, D., Toon, G. C., Blavier, J.-F. L., Washenfelder, R. A., Notholt, J., Connor, B. J., Griffith, D. W. T., Sherlock, V., and Wennberg, P. O.: The total carbon column observing network, Philos. T. R. S. A, 369, 2087–2112, https://doi.org/10.1098/rsta.2010.0240, 2011.

Zander, R., Rinsland, C. P., Farmer, C. B., Namkung, J., Norton, R. H., and Russell III, J. M.: Concentrations of carbonyl sulfide and hydrogen cyanide in the free upper troposphere and lower stratosphere deduced from ATMOS/Spacelab 3 infrared solar occultation spectra, J. Geophys. Res., 93, 1669–1678, https://doi.org/10.1029/JD093iD02p01669, 1988.